Article

Retrieving Secondary Forest Aboveground Biomass from Polarimetric ALOS-2 PALSAR-2 Data in the Brazilian Amazon

Henrique Luis Godinho Cassol 1*, Yosio Edemir Shimabukuro 1, Elisabete Caria Moraes 1, João Manuel de Brito Carreiras 2, Luiz Eduardo de Oliveira Cruz e Aragão 1, Camila Valéria de Jesus Silva 3, and Shaun Quegan 2

1 National Institute for Space Research (INPE) – Remote Sensing Division, Av. dos Astronautas 1758, Jd Granja, São José dos Campos, São Paulo, Brazil; henrique@dsr.inpe.br; yosio@dsr.inpe.br; bete@ltid.inpe.br; laragao@dsr.inpe.br.
2 National Centre for Earth Observation (NCEO), University of Sheffield, Western Bank, Sheffield, S10 2TN, UK; j.carreiras@sheffield.ac.uk; S.Quegan@shef.ac.uk.
3 Lancaster Environment Centre, Lancaster University, Lancaster, LA1 4YQ, UK; camilaflorestal@gmail.com.
* Correspondence: henrique@dsr.in.br; Tel.: +55-12-3208-6458

Abstract: Secondary forests (SF) are important carbon sinks, removing CO_2 from the atmosphere through the photosynthesis process and storing photosynthates in their aboveground live biomass (AGB). This process occurring at large-scales partially counteracts C emissions from land-use change, playing, hence, an important role in the global carbon cycle. The absorption rates of carbon in these forests depend on forest physiology, controlled by environmental and climatic conditions as well as on the past land use, which is rarely considered for retrieving AGB from remotely sensed data. In this context, the main goal of this study is to evaluate the potential of full polarimetric ALOS-2 PALSAR-2 data for estimating AGB by taking into account the past-land use of SF areas in the Brazilian Amazon. We surveyed a chronosequence of 42 SF plots (20 ha) near the Tapajós National Forest in Pará state to quantifying AGB growth rates. We explored the full polarimetric data testing three regression models including non-linear (NL), multiple linear regressions models (MLR), and the semi-empirical extended water cloud model (EWCM). The results showed that the intensity of previous use has affected the structure of SF by reducing the AGB accumulation and being noticeable by several polarimetric attributes. The combination of multiple prediction variables with MLR improved the AGB estimation by 70% comparing amongst other models (R^2 adj. = 0.51; RMSE = 13.2 Mg ha^{-1}) bias = 2.1 ± 37.9 Mg ha^{-1}. The error propagation of the MLR model was estimated to be 15%.

Keywords: backscattering; L-band; SAR polarimetry; microwave; Chapman-Richards model; tropical forest

1. Introduction

Secondary forests (SFs) are defined as areas of forests where clear cut was made only by anthropic actions, whether or not for conversion to other land uses [1]. Despite the multiples definitions of SFs fond in the literature [2, 3, 4, 5], hereafter, we consider as SF areas those that are in a process of regeneration after clearcutting Primary Forests (PFs) or SFs according to Convention on Biological Diversity CDB [1]. This definition was chosen because it adequately encompasses the classes of SF discriminated by satellite data on a regional or global scale [6].

According to Forest Resources Assessment FRA/FAO [7], from 106 nations located in the tropics, 36 have all remaining forests composed of SFs, almost half of all tropical countries have the majority of their forest land dominated by SFs, and only 19 of them have the dominance of PF in their territory, including Brazil. These numbers have led some authors to recognize the importance

of SFs, not only because of the capacity of these forests in maintaining biodiversity and mitigating anthropogenic carbon emissions, but also because SFs a likely to be the dominant state of rainforests in the future [2, 8, 9, 10, 11, 12].

Forests undergoing regeneration partially offset carbon emissions from land use change and fossil fuels by accumulating carbon in their biomass. It has been estimated that SFs have the potential to accumulate 0.86 Pg C yr^{-1} in Latin America [10]. This value is twice as large as carbon emissions from Land Use, Land-Use Change and Forestry (LULUCF), which accounts for 0.47 Pg C yr^{-1} [13]. In the Brazilian Amazon, estimates of C accumulation in SFs vary between 0.06 Pg C yr^{-1} [15] and 0.15 Pg C yr^{-1} [14]. Despite large uncertainties in these estimates, carbon uptake by SFs is likely to represent 17–44 % of total carbon emission from deforestation in the Brazilian Amazon. For improving these estimates, it is, therefore, crucial to accurately quantify the extent and growth rates of SFs in Amazonia [10, 13, 15, 16].

In the Brazilian Amazon, SFs covered between 140,000 km^2 and 228,000 km^2 until 2010 [19, 20, 22], representing approximately 30% of accumulated deforestation since 1988 (PRODES/INPE) [23]. The estimation of the extent of SF is often made using data from optical sensors [25, 26]. However, the low ability of these sensors in separating succession classes, confusion with other vegetation classes and the constant presence of clouds may reduce the accuracy of these estimates in tropical regions [24, 25]. To overcome these problems the analysis of time-series of land cover maps is essential for mapping SFs in the tropics to avoid misclassification [19]. These time-series also provide relevant information about prior land use history of each SF patch, including the period and type of land use before abandonment, the clear-cut frequency, and the fire history [19, 20, 24, 27]. This multi-temporal information is useful to model SF growth rates and to reduce the uncertainty of estimates throughout the Amazon region [18, 28].

Knowing the extent and biomass stocks of SFs is critical for modeling the impacts and feedbacks of climate change, by allowing a better representation of the magnitude of carbon assimilation in tropical forests. . Despite several quantifications of the areal extent of SFs have been done before, uncertainties still remain because of the above-mentioned limitations inherent of optical satellite sensors. Estimating forest biomass in these SFs, additionally, has been performed using Synthetic Aperture Radar (SAR) data because of two main reasons: avoidance of the effects of high frequency of cloud cover in tropical regions and sensitivity to biomass density values above 300 Mg ha^{-1} common in tropical forests with complex structures [19, 29, 30].

Forest AGB is usually estimated through regression models based on empirical relationships between AGB and radar parameters, including backscattering intensity or polarimetric decompositions [29, 30]. L-band SAR data is currently being used for AGB modeling, as the wavelength of its microwave pulse (23.5 cm) matches the dimensions of forest woody components. However, the sensitivity of L-band SAR data for estimating AGB is efficient until 100–150 Mg ha^{-1}, with saturation of the signal observed above these values [31]. To overcome this limitation, the use of multiple variables obtained from polarimetric decomposition has been proposed to describe these structurally complex environments [32, 33, 34]. Multiple linear regressions (MLR) have achieved $R^2 \approx 0.7$ for AGB prediction when using multiple variables from polarimetric decomposition [29, 32]. Furthermore, a new semi-empirical extended water cloud model (EWCM) has also been tested for AGB modeling [35, 37]. In this parametrization, AGB is inverted from the model by decomposing the backscattering in three elementary components obtained from the Freeman-Durden or Yamaguchi decompositions: odd-bounce, double-bounce, and volumetric [38]. The advantage of the EWCM model is to be insensitive of signal saturation to higher AGB values and the physical meaning of its β parameter [37]. Although these studies have retrieved AGB using polarimetric data, they were carried out only on PFs or using logarithmic models. So, the potential of polarimetric data for assessing AGB in SF is still rare in the literature.

Hence, the goal of this paper is to test the accuracy of AGB estimation in the SFs at the Santarem study site by analyzing polarimetric (quad-pol) data from the Advanced Land Observing Satellite-2 Phased Array L-band SAR-2 (ALOS-2 PALSAR-2). We used three regression models: nonlinear regression (NL), multiple linear regressions (MLR), and the semi-empirical EWCM. Moreover, we

Preprints (www.preprints.org) | NOT PEER-REVIEWED | Posted: 31 July 2018 doi:10.20944/preprints201807.0604.v1

also evaluate the use of ALOS-2 PALSAR-2 data to characterize SF according to land use intensity before abandonment. We expect that land use history would directly influence the shape of the relationship between parameters derived from the SAR data and forest biomass (structure of the SFs). Such analysis is designed to help us understand which parameters of SAR data are more related to forest regrowth pathways, improving the accuracy for estimating forest carbon stock and dynamics.

2. Materials and Methods

The study was carried out at the vicinity of the National Forest of Tapajós (FLONA Tapajós), hereafter described as the Santarém site, located 80 km south of the city of Santarém, Pará state. This site comprises an area of 1.118 km² and was part of the REGROWTH-BR project studying SFs of varying ages and subjected to different historical land use [20] (Figure 1).

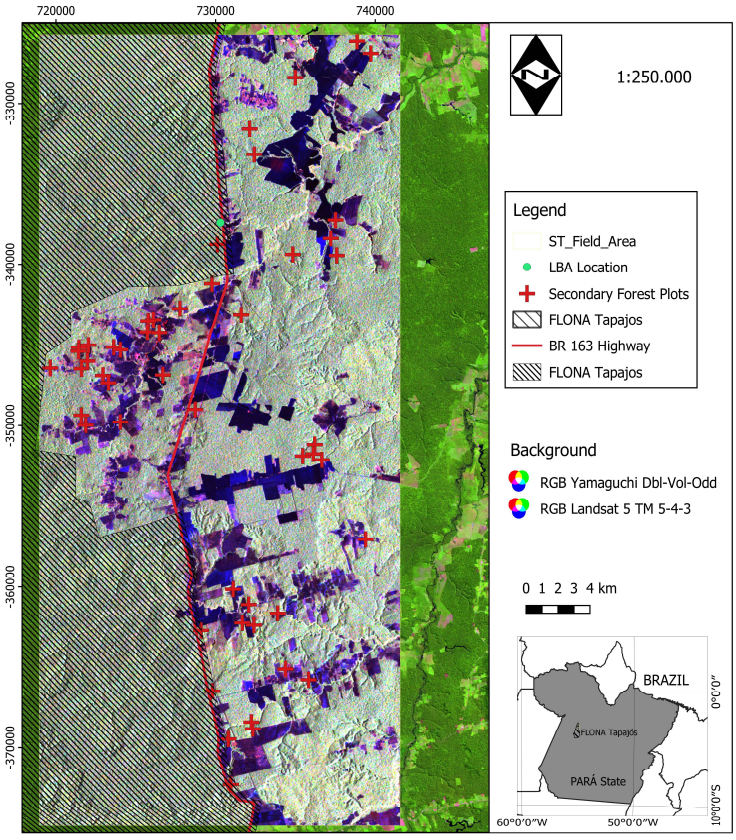

Figure 1. Site location and field plots inside the Regrowth-BR project (crosses). Background image is ALOS-2 PALSAR-2 color composite of Yamaguchi three scattering mechanisms: RGB/odd-bounce volumetric double-bounce. Red continuous line represents BR-163 highway, which connects city of Santarém, Pará State, and Cuiabá, Mato Grosso State. Optical background image is Landsat 5 TM Path/Row 227/69 of 29 Jun 2010.

2.1. A brief history of the ocupation in the Santarém region

Santarém has a long tradition in the production of raw materials from agriculture and forest extractivism [39]. Archaeological discoveries in this region showed continuous human activities that date back to 7000-8000 years-old [40]. When the Europeans arrived in Santarém in the 17th century, the region was already a complex center with a structure formed by several indigenous nuclei that practiced agriculture, trade and taxation [40].

Recently, the region underwent several agroforestry cycles: rubber (1924-1945), fiber production (1950s), and pepper (1970) [39]. At the beginning of the 21st century up to 2007 areas previously abandoned by slash-and-burn agriculture were deforested again, following

125 developmental programs to accelerate the soybeans outflow from the Midwest to the port of
126 Santarém with the paving of the BR-163 highway [41]. As a consequence of this "new occupation",
127 57% of the SFs in this study area are between 6-15 years old and have been deforested more than
128 three times since 1984 [20]. Besides that, Santarém has passed through severe droughts and forest
129 fires in 1998, 2005, 2010 and 2015, thus further changing the dynamics of land use and land cover
130 change [42].

131 *2.2. Site description*

132 The climate is classified as Am by Köppen climatic definition, with mean annual temperature
133 between 25.5 and 26.7 ^{0}C [43, 44]. According to Chave et al. [50], Santarém site is considered moist
134 forest located in areas with annual rainfall between 1500-2500 mm and dry season length < 5 months.
135 The dry season, considering average monthly rainfall lower than 100 mm, occurs from July to
136 November. The soils are predominantly Oxisols (red-yellow Latosols), with low cation exchange
137 capacity, high saturation by exchangeable aluminum Al+++, low pH, and are mainly found in
138 non-flooded upland *Terra-firme* areas [45]. In a lesser proportion than Oxisols, Ultisols (Argisols)
139 occurs in lowland and floodplain areas, which are also nutrient poor and often sandier [46, 47]. The
140 terrain is flat to undulate and the altitude is 100 m above sea level [49].
141 The vegetation prior to deforestation is classified as Dense Ombrophilous Forest of *Terra-firme*
142 and Open Rain Forest composed of palm trees in the sandy soils as *Attalea speciosa* Mart. (Babaçu)
143 and *A. maripa* (Aubl.) Mart. (Inajá) [51, 52, author's observations]. Dense Ombrophilous Forest of
144 *Terra-firme* presents a bi-modal distribution of tree-canopy height, one stratum formed by emergent
145 trees as *Manilkara huberi* (Ducke) Chev. (Maçaranduba) e *Hymanaea courbaril* L. (Jatobá) with an
146 average height of 35-40 m and a lower stratum made of sub-dominant trees (average height = 15-30
147 m) [53, 54, 55]. SFs, however, show an unimodal distribution of tree-height with mean 14.3 m where
148 emergent trees are rare and are represented by small individuals [58]. The species density ranged
149 between 133 and 186 sp ha^{-1}, and the tree density is 441 ± 43 ind ha^{-1} with the most predominant
150 families being Lechytidaceae and Fabaceae [43, 53, 54].

151 *2.3. Field and SAR data*

152 The processing steps of field inventory and ALOS-2 PALSAR-2 data processing are shown in
153 Figure 2 and are described in the following sections.
154

Preprints (www.preprints.org) | NOT PEER-REVIEWED | Posted: 31 July 2018 doi:10.20944/preprints201807.0604.v1

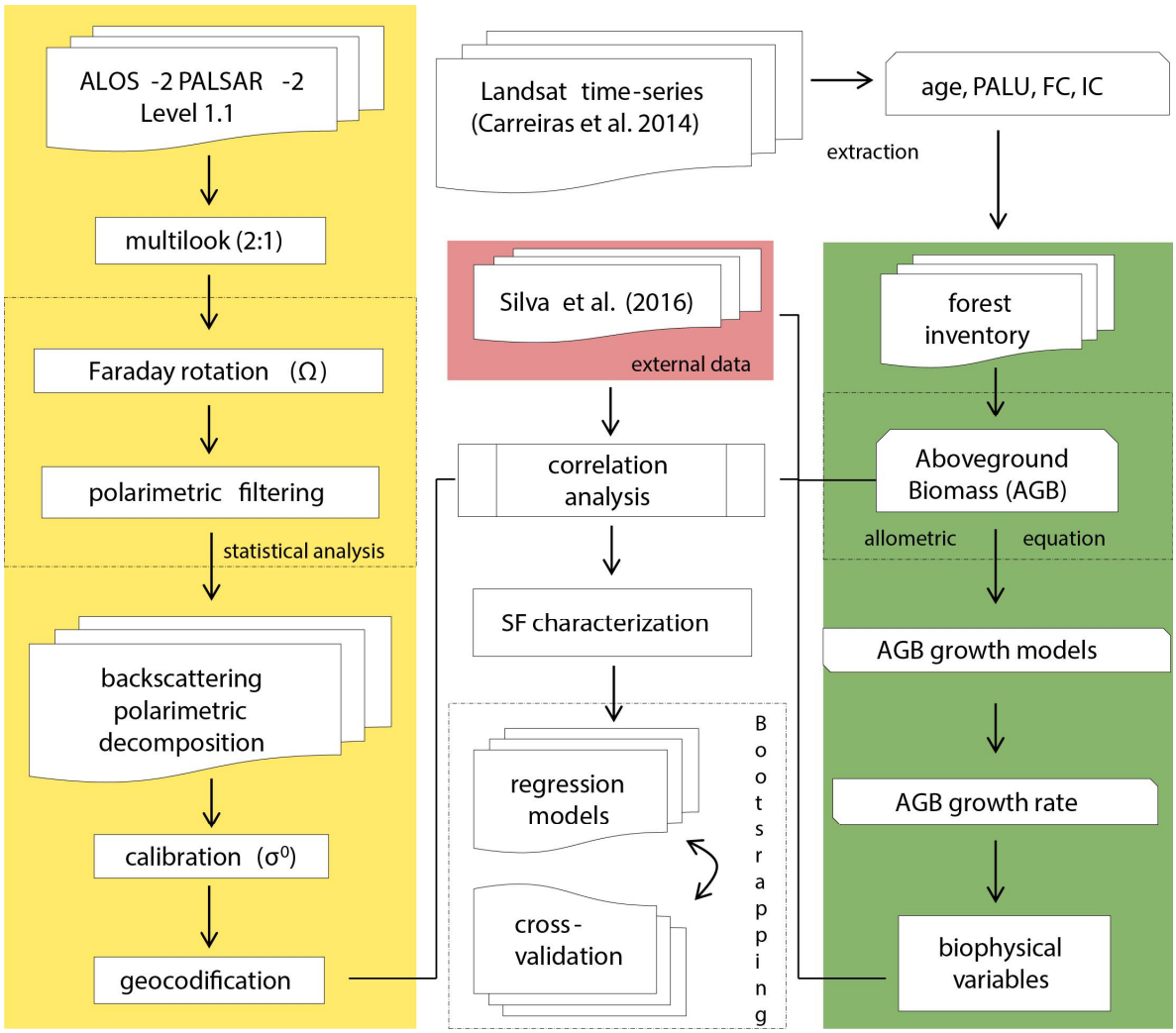

Figure 2. Methodological flowchart. Land use history of secondary forests (SFs) was obtained from the analysis of Landsat time-series [20], whereby were extracted the SF age, the period of active land use (PALU), the frequency of clear cuts (FC), and the intensity class of land use (IC). Field data processing following forest inventory to obtain biophysical parameters of SFs is highlighted in green. In yellow we summarize the processing steps of full-polarimetric SAR data. The methodology to characterize and to model AGB biomass in SFs is shown in the middle panel. Dashed boxes represent statistical analysis.

Landsat time-series were used to extract the land use history in SFs, such as age, period of active land use (PALU), and frequency of cuts (FC), and are described in Carreiras et al. [20]. SFs were then grouped into two classes of previous land-use intensity, referred to as intensity classes (ICs): IC = 1 when PALU ≤ 2 years and FC ≤ 2 times, or IC = 2 for PALU > 2 years or FC > 2 times.

Field plot data were composed by two databases: 16 plots measured in this study and 26 plots measured by Silva [57] (Table 1). The sample plots were placed close to the Tapajós National Forest (FLONA Tapajós, Pará State) on either side of the BR-163 highway, 100 km to the south of the Santarém city (Figure 1).

In this study we measured 16 nested plots of 60 x 100 m in advanced SFs (> 16 years) during September 2015. In the nested plots, all trees with a diameter at the breast height (DBH at 1.3 m height) greater than or equal to 5 cm were measured within a 10 × 100 m plot size. Trees with a DBH ≥ 10 cm were measured in a 20 × 100 m plot size, and trees with a DBH ≥ 20 cm were measured in a 60 × 100 m plot size.

Preprints (www.preprints.org) | NOT PEER-REVIEWED | Posted: 31 July 2018 doi:10.20944/preprints201807.0604.v1

Table 1. Field plot information by age, Diameter at Breast Height (DBH at 1.3 m height), area, and plot size.

N	Plot size (m)	DBH min (cm)	Age (years)	Area (ha)	Reference
16	10 x 100	5	16 - 28	1.60	Our study
16	20 x 100	10	16 - 28	3.20	Our study
16	60 x 100	20	16 - 28	9.60	Our study
14	20 x 50	5	1 - 7	1.75	Silva et al. [57]
9	20 x 50	5	7 - 16	2.40	Silva et al. [57]
3	25 x 100	10	> 16	1.35	Silva et al. [57]

Silva [56] carried out a field campaign between 2012 and 2013 at the same site. The method consisted of the collection of 23 plots (20 x 50 m) for the SF with initial and intermediate stages of succession and 3 plots for the advanced stages of succession (25 x 100 m). In both databases, all individuals were identified at the species level.

2.4. Aboveground biomass (AGB) allometric equations

The total AGB is composed by the sum of three components of the forest plots: living tree AGB, palm AGB, and standing dead tree AGB. Each of these components was addressed separately and has their own allometric equations for AGB estimation. The total AGB, hereafter named AGB, was then extrapolated to unit area (Mg ha^{-1}).

We evaluated 23 allometric equations to estimate AGB that are available from the literature for primary and secondary forests, and compared to the equations estimates with those from 148 harvested trees [59, 60]. All tested equations underestimated AGB, but the equation from Brown et al. [62] presented the lowest relative root mean square error (RMSE = 14%). The underestimation was due to the errors concerning individuals with DBH > 30 cm whose values were superior to 400 kg. Hence, living AGB was estimated with the equation developed by Brown et al. [62]:

$$AGB_{live} = \exp(-2.41 + 0.9522 \ln(\mathrm{DBH}^2\ h\ \rho)) \quad (1)$$

where AGB is the live aboveground biomass in kg, DBH in cm, h is the total height estimated by hypsometric equations adjusted by ecological species groups by Cassol et al. [58], and ϱ (rho) is the wood density collected from the literature and from the Global Wood Density Database [58, 61]. Palm AGB was measured with distinct equations according to Table 2.

Table 2. Equations to estimate the above-ground biomass (AGB) of palm trees.

Species	AGB Equation	Nº	Reference
Astrocaryum aculeatum G.Mey., *Euterpe precatoria* Mart., *Oenocarpus minor* Mart., *Syagrus inajai* (Spruce) Becc., *S. coccoides* Mart.	$AGB_{palm} = 0.399 + 7.907\ h$	(2)	[63]
Astrocaryum vulgare Mart	$AGB_{palm} = 21.302\ h$	(3)	[64]
Attalea maripa (Aubl.) Mart. and *A. speciosa* Mart.	$AGB_{palm} = \exp(3.257 + 1.125 \ln(h + 1))$	(4)	[64]
Elaeis oleifera (Kunth) Cortés	$AGB_{palm} = (0.55512\ (h\ \mathrm{DBH}^2\ \varrho)^{0.25})^4\ h$	(5)	[64]
Oenocarpus bacaba Mart.	$AGB_{palm} = \exp(4.5496 + 0.1387\ h)$	(6)	[64]

The AGB of standing dead trees was estimated with (1) using a rotten wood density ϱ = 0.342 g cm^{-3} and with (5) for dead palms using ϱ = 0.327 g cm^{-3} [65].

SF plots provided by Silva et al. 2016 had their AGB estimated by Uhl equation [66]:

$$AGB_{live} = \exp(-2.17 + 1.02 \ln(\mathrm{DBH}^2) + 0.39 \ln(h)) \quad (7)$$

 doi:10.20944/preprints201807.0604.v1

2.5. Growth models for biophysical variables

The objective of modeling secondary forest growth was to project the estimates of those biophysical variables to the SAR acquisition date in order to avoid temporal mismatch between both datasets, and also to provide the accumulation rates of these variables by age. Otherwise, the data from SAR may be not representative of the structural biophysical parameters presented on SFs. The biophysical parameters modeled were: mean diameter (DBH), mean total height (Ht), basal area (G), tree density (N), number of species per hectare (S) and total aboveground biomass (AGB). The selected growth yield model was Chapman-Richards (8):

$$Y_t = A(1 - e^{-kt})^c + \varepsilon \quad (8)$$

where Yt represents the size of the variable at age t; A refers to the asymptote (maximum value of Y as age tends to infinite), the coefficient k is the growth rate of Y as a function of time t, c is the shape of the curve (inflection point), and ε is the experimental error. The negative exponential was used to estimate N (9) as [17]:

$$N = N_a + (N_0 - N_a).e^{-kt} + \varepsilon \quad (9)$$

where N_0 is the asymptote (number of individuals per hectare at t = 0), N_a is the number of individuals per hectare at t = ∞, k is the decrease rate of N at time t. The parameters of the (8) and (9) were adjusted using the non-linear least squares method [67].

The input data for the growth models were obtained from SFs data located in Santarém region with ages varying from 1 to 30 years, along with field plots measured in the present study [68, 69, 70]. Plots obtained from these studies vary according to size, age, and methodology of measurement, but were carried out under similar environmental conditions (same geographic location) - 1st model assumption. However, the high variability of the dataset may result in the non-convergence of the growth model parameters; and a simple solution is to hold fixed one of its parameters [71]. Thus, a fixed value was assumed for the asymptote (A, N or N_0) of each biophysical parameter whereby we assumed that SF reaches resembling values of adjacent PF - 2nd model assumption [17]. These maximum values were obtained from the literature and correspond to the mean value observed in the PFs located nearby the study area (Table 3). The goodness-of-fit of the Chapman-Richards models was evaluated by the significance and the confidence interval of their parameters, as well as by the visual analysis of their residuals [72].

Table 3. Asymptote of the biophysical parameters in the primary forest used for modeling the secondary forest growth.

Biophysical parameters	Asymptote	Units	References
Mean diameter (DBH)	23.1	cm	17, 49, 56, 75, 77, 81, 82, 83
Mean total tree height (Ht)	25.0	m	17, 56, 78, 81, 85
Basal area (G)	24.4	$m^2\ ha^{-1}$	17, 56, 73, 74, 76, 78, 80, 81, 84
Species richness (S)	133.00	$sp\ ha^{-1}$	53
Tree density (N)	433.00	$individuals\ ha^{-1}$	17, 53, 74, 75, 80, 81, 84
Aboveground biomass (ABG)	314.00	$Mg\ ha^{-1}$	17, 53, 54, 56, 86

From the adjusted models, the accumulation rates of the SFs were obtained through the partial derivatives of the AGB model. The mean annual increment (MAI) was obtained by the derivative of the second order, or simply by dividing the estimated value by the corresponding age [87]. The age at which SF growth rate is maximum (maximum MAI) was then estimated according to the MAI curves.

2.6. ALOS-2 PALSAR-2 data processing

Two full-polarimetric scenes covering the study site were acquired in CEOS SAR format single look complex (SLC) at processing level 1.1 in slant range and HBQ mode of acquisition (High

Sensitive). SAR images were acquired at descending orbit in a right-looking off nadir angle (θ) of 28-31°. The SLC nominal resolution is 2.86 m and 3.13 m in range and azimuth respectively. Both scenes were acquired at the end of rainy season (6 February 2015). The cumulative rainfall on the date of acquisition and the day before was 10 mm [89]. The low accumulated precipitation at the previous date, however, should not cause major problems related to the increase in dielectric constant given the high evaporation in this season (about 3.5 mm day^{-1}), whereby partially cancels the cumulative precipitation.

In orbital low-frequency SAR systems, the path of the microwave pulse traverses twice the ionosphere, a region of free electrons pervaded by the magnetosphere resulting in the rotation of the plane of the polarization wave, known as Faraday Rotation (FR) [90]. The magnitude of the FR depends on a number of factors, including RADAR wavelength, degree of ionization, solar activity, geographic position, and total electron content (TEC) at the acquisition date. The TEC is defined as amount of free electrons in the ionosphere magnetic field and causes an increase in the FR angle (Ω). Due to intense solar activity, the TEC observed at the acquisition date was high, *circa* 70 x 10^{16} electrons m^{-2}, which resulted in a FR angle of approximately 15° in the plane of transmitted wave polarization and around 30° considering the transmitted and received wave [90, 91, 92]. According to Wright et al. [92], angles of rotation greater than 8.3° may reduce the accuracy of biophysical parameters estimation. FR was previously corrected in one scene, but preliminary analysis of the corrected data showed no significant changes in the polarimetric responses of the main forest targets. So, we did not perform FR correction in order to avoid unnecessary transformation of the coherence matrix, although we believe this correction is necessary when data from different orbits and dates will be used, or for classification purposes.

Image processing consisted of the following procedures: multilooking, polarimetric filtering, extraction of attributes derived from covariance and coherency matrices, polarimetric decompositions, calibration, and finally geocoding (Figure 2).

The azimuth and range resampling factor (multilooking) was set at 2:1, resulting in a nominal spatial resolution of approximately 6.25 m squared pixel. Although multilooking is a process of de-speckling, we also performed a polarimetric filtering to further reduce speckle noise.

Since the size of the forest plots are several orders of magnitude greater than the SAR spatial resolution (10-15 times), we have tested different filter sizes with the objective of finding the most suitable window size for de-speckling. So, we used a Refined Lee polarimetric filter, testing ten different filter sizes, from 3x3 to 21x21 pixels and compared the resulting mean intensity backscattering in all polarizations with the AGB from field data. The optimal window size was set up to 11 x 11 pixels, selected by looking at the mean relative growth of R^2 between filters of different sizes and the AGB at plot level (Figure 3). This optimal window size was a trade-off between the gain obtained by the de-speckling caused by indiscriminate increase of the filter size and the loss of relevant radiometric information caused by smoothing [59].

Preprints (www.preprints.org) | NOT PEER-REVIEWED | Posted: 31 July 2018 doi:10.20944/preprints201807.0604.v1

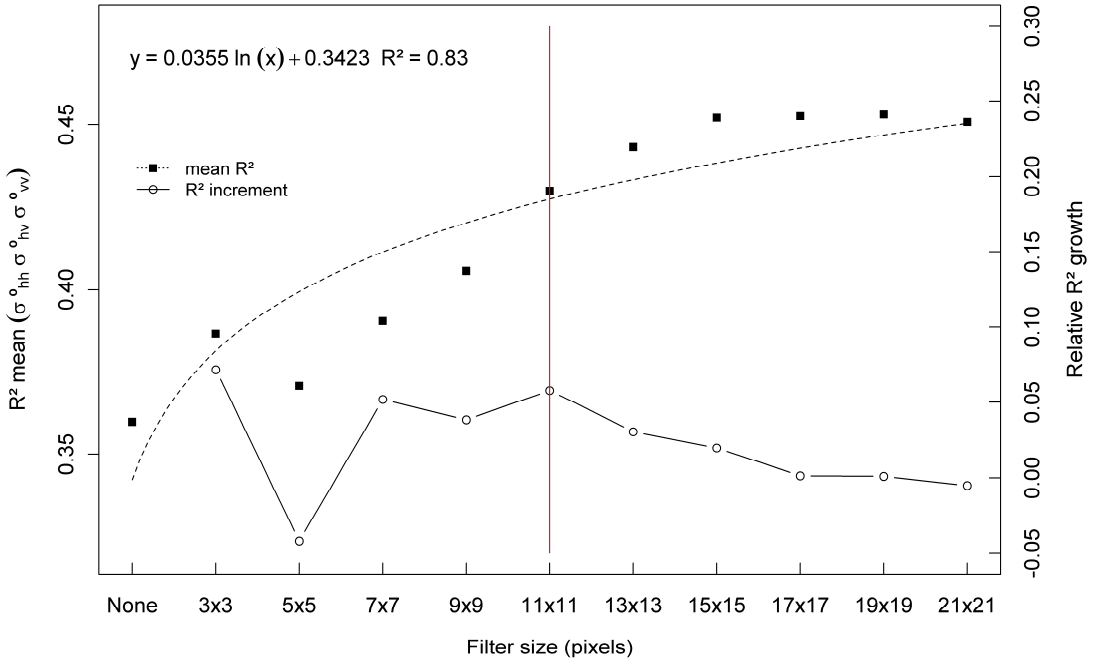

Figure 3. Coefficient of determination between mean HH, HV and VV backscatter and AGB by filter size (main axis). Relative growth of R^2 by filter size unitless (secondary axis).

Several attributes from the coherency and covariance matrices and polarimetric decompositions were obtained for characterizing SF by ICs and for modeling forest AGB. PolSARpro 5 (https://earth.esa.int/web/polsarpro/home) was used to generate 125 polarimetric attributes (Table A.1, Appendix A).

Calibration consists of converting digital numbers (DN) to backscatter coefficient σ (sigma-naught, in dB) in the four polarizations, and is calculated by (10) [88]:

$$\sigma^{\circ} = 10 \log10 (I^2 + Q^2) + CF \quad (10)$$

where I and Q are the phase image and complex image phase quadrature (SLC), respectively. CF is the calibration coefficient factor CF = -83 dB ± 0.406 dB [88].

After calibration and extraction of the polarimetric attributes, data was geocoded using the Range-Doppler approach. This process performs geocoding of the SAR data with precise transformation of slant-range to ground-range using a Digital Elevation Model (DEM) [93, 94]. In addition to obtaining precise geocoding, topographic effects are reduced in the estimation of backscatter coefficients, which is considered a source of uncertainty for AGB estimation [29, 95].

2.7. Correlation analisys

Correlation analysis was performed to find the best subset of polarimetric attributes to be used in the regression model. Furthermore, the correlation was also used to find the best polarimetric attributes which allow separate SFs by intensity classes (IC).

A correlation-based feature selection (CFS) filter algorithm [96] was applied in order to reduce the dimensionality of the data. This was implemented in R with the FSelector package [97]. In the CFS approach an algorithm selects a subset of attributes based on the correlation coefficients and the concept of information entropy theory. The metrics of Yang and Pedersen [98], such as information gain and chi-square test (χ^2), were used to measure the degree of association between the class of intensity used and the attributes, as well as the interrelationship among attributes. The best subset of data is formed by the attributes having higher correlation and greater gain of information with the class and having also lower correlation amongst them [96, 99].

Preprints (www.preprints.org) | NOT PEER-REVIEWED | Posted: 31 July 2018 doi:10.20944/preprints201807.0604.v1

Data was randomized into 10 subsets by the leave-one-out cross-validation process and the result of the best subset of polarimetric attributes was generated. The polarimetric attributes that appeared in 50% or more cases were selected.

2.8. Models to retrieve aboveground biomass

We evaluated the performance of three different types of regression models for AGB estimation: i) non-linear, ii) multiple linear; and iii) semi-empirical EWCM. Goodness-of-fit was calculated using i) the significance and confidence interval of the regression parameters, ii) the distribution of the standardized residuals from the regression to verify the presence of possible outliers; (iii) the Akaike information criterion (AIC), and iv) the Breusch-Pagan test to evaluate the homoscedasticity of the residuals [72].

2.8.1. Non-Linear Regression Model

The non-linear regression model involves the logarithmic relationship between AGB (Y) and a single independent variable (X), usually the backscatter coefficient, given by (11):

$$Y_i = E(Y_i|X_i) + \varepsilon_i = f(X_i, \theta_i) + \varepsilon_i \quad (11)$$

whereby the average of the *i-th* observations $E(Y_i|X_i)$ depend on X_i, by means of a mean kernel function of $f(X_i, \theta_i)$; X_i is the explanatory variable that can have one or more components and θ_i is the parameter vector. ε_i is the random error with mean $E\{\varepsilon_i\} = 0$ and variance $\sigma^2\{\varepsilon_i\} = \sigma^2/w$ by the non-linear least squares method. For many practical applications, w, which is the weight given to the variance, is equal to one. Nonlinear models were fit with the "nls" package in R.

2.8.2. Multiple Linear Regression Model

In a multiple linear regression model, the dependent variable AGB (Y) is estimated by multiple independent variables (X) from the SAR data by a linear (in the parameters) relationship with these variables (12):

$$Y_i = \beta_0 + \beta_1 X_{i1} + \beta_2 X_{i2} + \cdots + \beta_{p-1} X_{i,p-1} + \varepsilon_i \quad (12)$$

where Y_i is AGB at the *i-th* observation in Mg ha^{-1}, β_0, β_1, ..., $\beta_{(p-1)}$ are the model parameters and $X_{i,p-1}$ are the p-1 explanatory variables at the *i-th* observation, and ε_i is the random error with mean $E\{\varepsilon_i\} = 0$ and variance $\sigma^2\{\varepsilon_i\} = \sigma^2$.

In MLR the shape and orientation of multiple scattering mechanisms and other parameters of SAR decomposition in one resolution cell can be used instead of only the backscattering coefficient. However, MLR can have some limitations, namely in terms of parameter interpretation and overfitting.

Multiple linear models were fit with the ordinary least squares (OLS) method. The analysis was performed using the exhaustive selection package "Glmulti" implemented in R [101]. The selection of the model was performed by the AIC criterion, whose models with Δ AIC < 2 were chosen; and the best model was determined by the weights given to the set of explanatory variables in the model. The larger the weight, the greater is the contribution of each variable to the model. The selection of optimal subset was performed by CFS selector in order to reduce the input polarimetric attributes avoid overfitting in the MLR [72].

2.8.3. Semi-empirical Model EWCM

The EWCM is an adaptation of the radiative transfer model developed by Attema and Ulaby [36] that expresses the relation between the backscattered signals by the multiple scattering elements in a horizontal homogeneous medium, the cloud droplets. According to the EWCM, incoming electromagnetic waves are the result of the energy partially reflected directly by the vegetation and the transmitted energy of the lower vegetation layers which suffers attenuation by multiple scatters

Preprints (www.preprints.org) | NOT PEER-REVIEWED | Posted: 31 July 2018 doi:10.20944/preprints201807.0604.v1

before returning to the sensor. Hence, the backscatter coefficient of a forested area is a result of backscatter coefficients from vegetation, ground, and ground-stem interaction, given by Eq. (13) [37]:

$$\sigma^o_{for} = (1-A)\sigma^o_{gr} + A\sigma^o_{gr}T_{tree} + A\sigma^o_{veg}(1-T_{tree}) + (1-A)\sigma^o_{gs} + A\sigma^o_{gs}T_{tree} \quad (13)$$

where σ^o_{for} is the total backscatter coefficient of the forest, in dB; σ^o_{gr} is the backscattering coefficient of the ground from canopy gaps; σ^o_{veg} is the backscattering coefficient of vegetation; σ^o_{gs} is the backscatter from the ground-stem interaction, A is the fraction of the forest area illuminated by the SAR observation and T_{tree} is the two-way transmissivity resulting from the trees.

The term T_{tree} is the amount of total energy transmitted to the lower canopy layers, expressed as the inverse exponential attenuation per meter "α" of the product of two directions in a forest layer of thickness "h", as $T_{tree} = e^{-\alpha h}$ [102]. Thus, equation (13) can be rewritten as (14):

$$\sigma^o_{for} = \sigma^o_{gr}(1-A+Ae^{-\alpha h}) + A\sigma^o_{veg}(1-e^{-\alpha h}) + A\sigma^o_{gs}(1-A+Ae^{-\alpha h}) \quad (14)$$

The two-way transmissivity attenuation of the forest can be expressed in terms of A as $T_{for} = (1-A+Ae^{-\alpha h})$, and is related to the amount of scatters present in the area, in an empirical relation with AGB as (15) [35]:

$$\sigma^o_{for} = \sigma^o_{gr}e^{-\beta AGB} + \sigma^o_{veg}(1-e^{-\beta AGB}) + \sigma^o_{gs}e^{-\beta AGB} \quad (15)$$

where AGB is the above-ground biomass, in Mg ha^{-1} and β is the empirical coefficient of attenuation as a function of AGB.

The backscatter coefficients resulting from ground, vegetation and ground stem interaction can be replaced by the uncorrelated scattering mechanisms from the Freeman and Durden or Yamaguchi polarimetric decompositions, for instance, as surface (odd-bounce), volumetric and double-bounce, respectively [37]. Then, by inverting (15), AGB can be modeled by means of the scattering mechanisms as in (16):

$$AGB = -\frac{1}{\beta}\left[\ln\frac{(P-P_v)}{(P_s-P_v+P_d)}\right] \quad (16)$$

where P is the total power (span) represented by the sum of the three scattering mechanisms in linear units, P_v is the volumetric scattering and represents the backscatter of the forest canopy σ^o_{veg}, P_s is the surface scattering and is related to the direct backscatter of the ground σ^o_{gr}, and P_d is the double-bounce scattering resulting from the backscatter of the ground stem interaction [37]. To feed the model, the most correlated decompositions with AGB were tested, but Yamaguchi's was used because it was less sensitive to changes in the orientation angle.

2.9. Evaluation of model's performance

Validation of the regression models was carried out by assessing the distribution and coefficient of determination (R^2) between predicted and reference values (from the validation sample) and by the root mean square error and its bias and variance terms [100] (17):

$$RMSE = \sqrt{bias^2 + \text{variance}} \quad (17)$$

In addition, the error distribution was presented for each model and null hypothesis of the deviation (bias) of the estimate to be equal to zero (without trend) was analyzed by the one-sample t-test. The number of plots was small (n = 42), thus limiting the separation in training and validation subsets. Therefore, a bootstrapping randomization process with 100 repetitions was carried out, maintaining the separation of 80% for training and 20% for validation.

3. Results

3.1. Structural parameters of secondary forests

Almost half of the plots had a high intensity of use before abandonment (IC = 2). As expected, the maximum AGB found in our sampling was observed at a 28 years old secondary forest plot

Preprints (www.preprints.org) | NOT PEER-REVIEWED | Posted: 31 July 2018 doi:10.20944/preprints201807.0604.v1

(AGB = 200.0 Mg ha^{-1}). Mean AGB in the initial secondary succession class (ISS) is less than half when compared to the mean value of the advanced secondary succession class (Table 4).

Table 4. Mean and standard deviation (in brackets) of structural parameters in secondary forest plots by succession class: ISS – initial secondary succession, IntSS – intermediate secondary succession, and AdvSS - advanced secondary succession, and IC - Intensity Classes. The abbreviations are: FC - frequency of cuts, PALU - period of active land-use, DBH - diameter at the breast height, Ht - total height, G - basal area, S – species density, N – tree density, AGB - aboveground biomass.

Plot	n (plots)	Age* (years)	FC (x)	PALU (years)	DBH (cm)	Ht (m)	G (m² ha^{-1})	S (sp ha^{-1})	N (ind ha^{-1})	AGB (Mg ha^{-1})
IC = 1	**22**	**16.5(6.8)**	**1.6(0.5)**	**1.4(0.5)**	**16.2(2.9)**	**14.8(1.2)**	**22.1(5.6)**	**45(11)**	**1036(325)**	**129.4(47.6)**
ISS	3	3.7(0.6)	1.7(0.6)	1.7(0.6)	12.6(2.6)	13.3(1.3)	15.6(5.1)	31(9)	805(137)	71.2(41.4)
IntSS	4	11.0(2.0)	1.8(0.5)	1.0(0.0)	13.0(1.3)	13.6(0.6)	17.0(2.9)	32(4)	778(71)	74.9(18.5)
Adv	15	20.5(2.6)	1.5(0.5)	1.4(0.5)	17.7(1.7)	15.4(0.7)	24.8(4.1)	51(6)	1151(332)	155.6(27.9)
IC = 2	**20**	**7.5(6.2)**	**3.0(1.1)**	**3.3(1.7)**	**12.5(2.6)**	**13.2(1.3)**	**16.6(6.4)**	**32(9)**	**1013(428)**	**77.2(43.1)**
ISS	11	3.2(1.2)	3.1(1.2)	3.5(1.7)	11.7(2.9)	12.9(1.5)	13.6(5.9)	28(10)	851(152)	62.0(42.4)
IntSS	5	7.8(1.3)	2.6(1.3)	4.2(1.3)	12.8(1.0)	13.4(0.5)	16.5(2.0)	31(3)	791(52)	70.8(15.8)
Adv	4	18.8(1.7)	3.3(0.5)	1.5(0.6)	14.4(2.5)	13.6(1.3)	25.2(3.2)	43(6)	1735(456)	126.9(35.2)
Mean	**42**	**12.2(7.9)**	**2.3(1.1)**	**2.3(1.5)**	**14.4(3.3)**	**14(1.5)**	**19.5(6.5)**	**39(12)**	**1025(373)**	**104.5(52.2)**

Note: * Age at the field survey.

3.1. Growth models and accumulation rates of the secondary forests biophysical parameters

The curves of biophysical parameters showed different behavior, indicating distinct accumulation rates. The fitted growth models for mean DBH, mean tree height, and species density do not show a typical sigmoidal shape, but resembles logarithmic models - inflection point $c < 1$ (Figure 4). As a consequence, the corresponding maximum MAI occurs very early. All model parameters (A, k and C) were significant for $\alpha = 0.05$. For instance, mean DBH and mean tree height showed a rapid growth in the SFs of Santarém reaching half of the PF value in approximately 9 and 8 years, respectively (Figure 4 A-B). The MAI of mean DBH was higher than 2 cm yr^{-1} in the first 5 years (Figure 4 A). The MAI of mean tree height was greater than 1 m yr^{-1} during the first 13-14 years (Figure 4 B), with similar results reported by Neeff and Santos [17].

The basal area was the biophysical parameter that reached the asymptote faster in the SFs, as reported by others authors [12, 103]. For instance, SFs recover 90% of G observed in adjacent PF at 19 years age (Figure 4 C). The maximum MAI estimated was 1.6 m² ha^{-1} yr^{-1} and occurred in the fourth year, while [17] observed maximum MAI in the sixth year. Along with the Ht and G, the tree density quickly reaches values close to the PFs [17, 103]. At the age of 20, the SF presents 70% of the tree density per hectare of the PF (Figure 4E). Due to different measurements methodologies, we excluded some advanced SF aging plots > 20 years in the analysis of tree density.

The number of species, on the other hand, showed slowest accumulation in the SFs among biophysical parameters; the MAI was below to 4 sp ha^{-1} yr^{-1} in the first 10 years and inferior to 2 sp ha^{-1} yr^{-1} from the age of 25 years (Figure 4D). In this species recover rate, the SFs of the Santarém site would present 72% of the number of species per average hectare observed in the PF at approximately 100 years.

The mean AGB showed intermediate recovering rate among biophysical variables. The mean annual increment occurs at 18th year MAI = 6.6 Mg ha^{-1} yr^{-1} (Figure 4F). At this growth rate, 50% of the asymptote is reached at age 25; and 75% at age 44. Considering that approximately 50% of the AGB is organic carbon (C), the potential assimilation of C is greater than 3.7 Mg C ha^{-1} yr^{-1} in the Santarém SF up to 10 years.

Preprints (www.preprints.org) | NOT PEER-REVIEWED | Posted: 31 July 2018 doi:10.20944/preprints201807.0604.v1

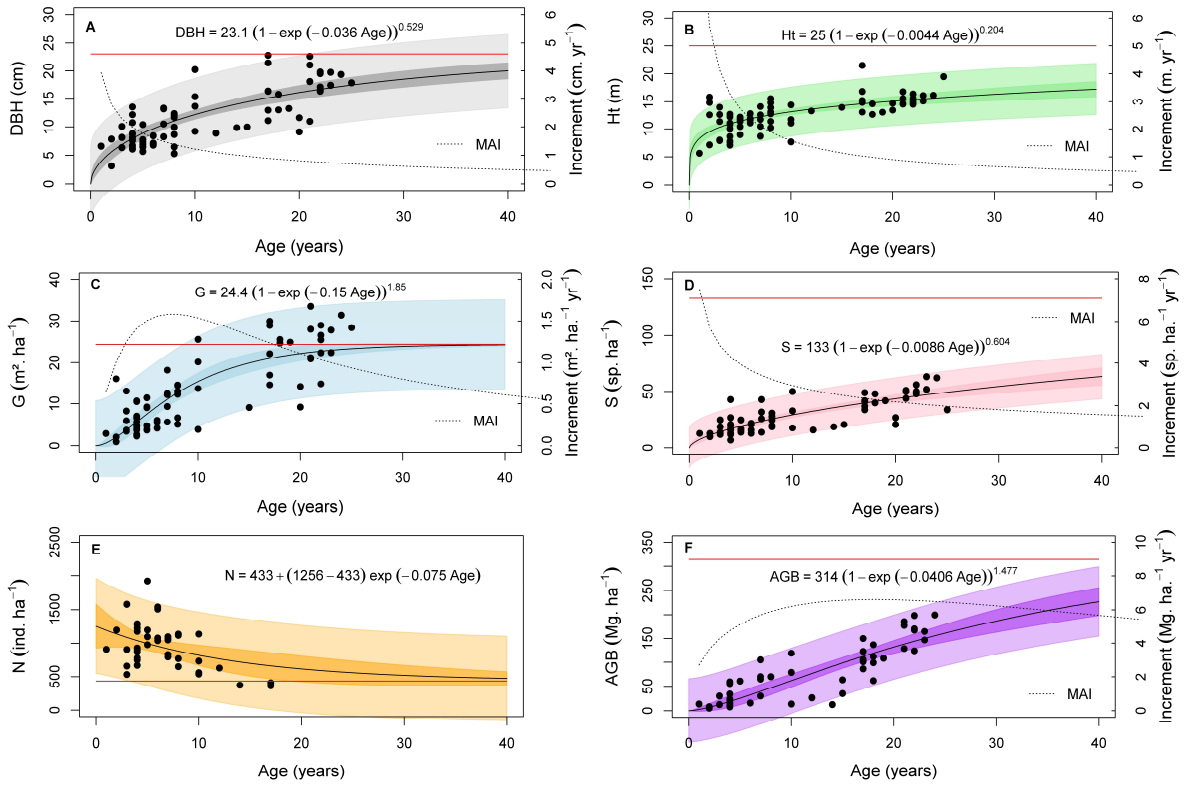

Figure 4. Growth models of mean diameter at breast height (A), mean tree height (B), basal area (C), species density (D), tree density (E), and aboveground biomass (F) in Santarém site by age of secondary forests (continuous black line). Secondary axis represents the relative growth per year (increment). The continuous red line refers to primary forest asymptote. Confidence and prediction intervals are represented in dark and light shaded areas, respectively. Dashed line represents the mean annual increment (MAI).

3.2. Distribution of biophysical variables after modeling growth

The fitted growth models described in the previous section were used to predict the biophysical variables to the date of ALOS-2 PALSAR-2 data acquisition. All biophysical variables follow a normal distribution with this being significantly different in terms of IC (t-test, $\alpha = 0.05$), apart from tree density (Figure 5). Secondary forests abandoned after light intensity use (IC = 1) had higher values of biophysical parameters when compared to those from SFs subjected to heavy intensity use (IC = 2).

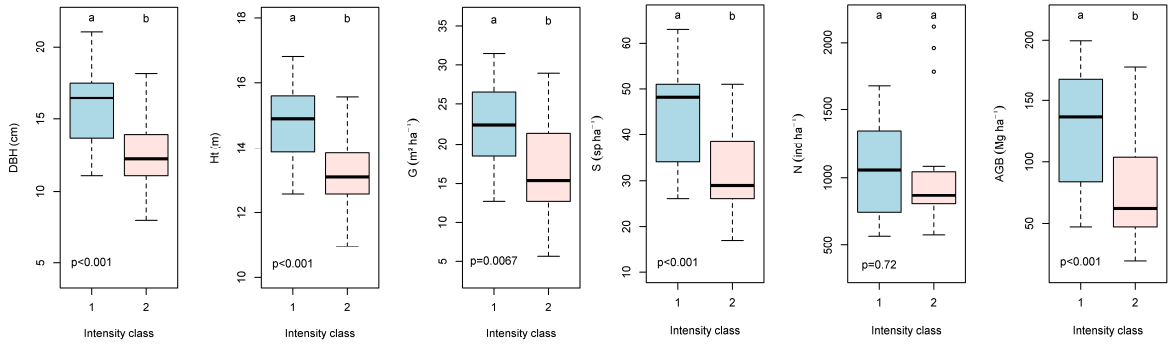

Figure 5. Distribution of biophysical variables: mean diameter at breast height (DBH), mean tree height (Ht), basal area (G), species density (S), tree density (N), and aboveground biomass (AGB) by intensity class of previous use in the secondary forests of Santarém study site after modeling growth.

Preprints (www.preprints.org) | NOT PEER-REVIEWED | Posted: 31 July 2018 doi:10.20944/preprints201807.0604.v1

3.3. Characterization of secondary forest with polarimetric data

According to the CFS selection criteria, only four polarimetric attributes were selected in more than 50% of the subsets when separating SFs by intensity classes of use (Table 5). They were the real terms C_{12} and T_{13} of the covariance $[C]_3$ and coherence $[T]_3$ matrices, the diagonal term T_{22} of the Cloude coherence matrix, and the imaginary term T_{23} of the Barnes-Holm decomposition (Table 5). However, the last term T_{13_real} did not present significant differences by the W-test between ICs.

Table 5. Polarimetric attributes selected by CFS criteria for separation of the SF by intensity classes using the 10:1 cross validation. The Normal distribution attributes follow two sample t-test and non-normal Wilcoxon W-test.

Attribute	% of CFS selected attributes	p-value (t –test or W)
I_C12real	90	t: 0.017
T13_real	70	W: 0.110
T22_C	60	t: 0.022
T23_imagB	60	W: 0.021
T22	50	W:0.026
TVSM_phi_s	50	t: 0.018
MCSM_Wire	50	W: 0.012
MCSM_Dbl	50	W: 0.042
l3	50	W: 0.018
Yamaguchi_Dbl	50	t: 0.025
…	…	…

Note: I_C12real - real term off diagonal of the covariance matrix $C_{12} = \sqrt{2}\langle S_{HH}S_{HV}^{*}\rangle$, T13_real - real term off diagonal of the coherency matrix $T_{13} = \langle (S_{HH} + S_{VV})S_{HV}^{*}\rangle$, T22_C - relative difference between the co-polarized channels of coherency matrix from Cloude $T_{22}C = \langle |S_{HH} - S_{VV}|^2\rangle$, T23_imagB – imaginary term off diagonal of the Barnes-Holm coherency matrix $T_{23}B = \langle (S_{HH} + S_{VV})S_{HV}^{*}\rangle$, T22 - relative difference between the co-polarized channels of coherency matrix $T_{22} = \langle |S_{HH} - S_{VV}|^2\rangle$, TVSM_phi_s - Touzi phase module angle, MCSM_Wire - Zhang wire scattering mechanism, MCSM_Dbl - Zhang double-bounce scattering mechanism, l3 - third eigenvalue associated to the respective eigenvector of the Cloude decomposition, and Yamaguchi_Dbl - Yamaguchi double-bounce scattering mechanism.

Those ten attributes were significant at α = 0.05 significance level in the correlation analysis with intensity class, a part of T_{22_C} significant at α = 0.1, and are related to distinct biophysical variables (Figure 6). The biophysical variables were negative correlated with IC's meaning that areas of SF that suffered intense land use exhibit lower biophysical values, but the period of active use and frequency of cuts were positively correlated with IC (ϱ = 0.62-0.63, Figure 6). From this analysis, we inferred that DBH and Ht were more related to ICs than AGB (ϱ = -0.56, and ϱ = -0.48, Figure 6).

The highest correlation value with IC (ϱ = 0.56), the real term off the diagonal of the covariance matrix $C_{12} = \sqrt{2}\langle S_{HH}S_{HV}^{*}\rangle$, showed non-significant correlation values with any of the biophysical variables tested. This term is a measure of the complex coherence degree between HH and HV channels, whereby values close to zero representing targets with low polarimetric coherence; and values close to one, representing targets with highest polarimetric coherence [111]. Areas of SFs intensively used in the past IC = 2 showed low complex coherence (Figure 7). The term T_{13_real} also showed no significant correlation with any biophysical variable.

SFs areas of IC = 1 have higher values of polarimetric attributes that have direct relation with volumetric and canopy scattering, as the attribute T_{22} T_{22_C}, and λ_3, as well as with wire and double-bounce scattering mechanisms (MCSM and Yamaguchi). T_{22}, the term representing the relative difference between the co-polarized channels (HH and VV), is associated with the double-bounce metric. λ_3, which refers to the third eigenvalue, represents the magnitude of the cross-polarization signal (HV) associated to the respective eigenvector of the Cloude decomposition. These higher values of T_{22} T_{22_C}, and λ_3 are expected for more structured forests and with higher AGB,

Preprints (www.preprints.org) | NOT PEER-REVIEWED | Posted: 31 July 2018 doi:10.20944/preprints201807.0604.v1

as is the case of abandoned SFs after cutting (IC = 1). The wire scattering mechanism is predominant in urban environments and results from the interaction of the electro-magnetic waves with edges, eaves and window frames [113]. Obviously, these structures are not present in forests, but according to the authors themselves, these elementary mechanisms are manifested when the condition of reflection symmetry is not satisfied and the terms outside the main diagonal of the covariance matrix are not zero, which is be the case of SF.

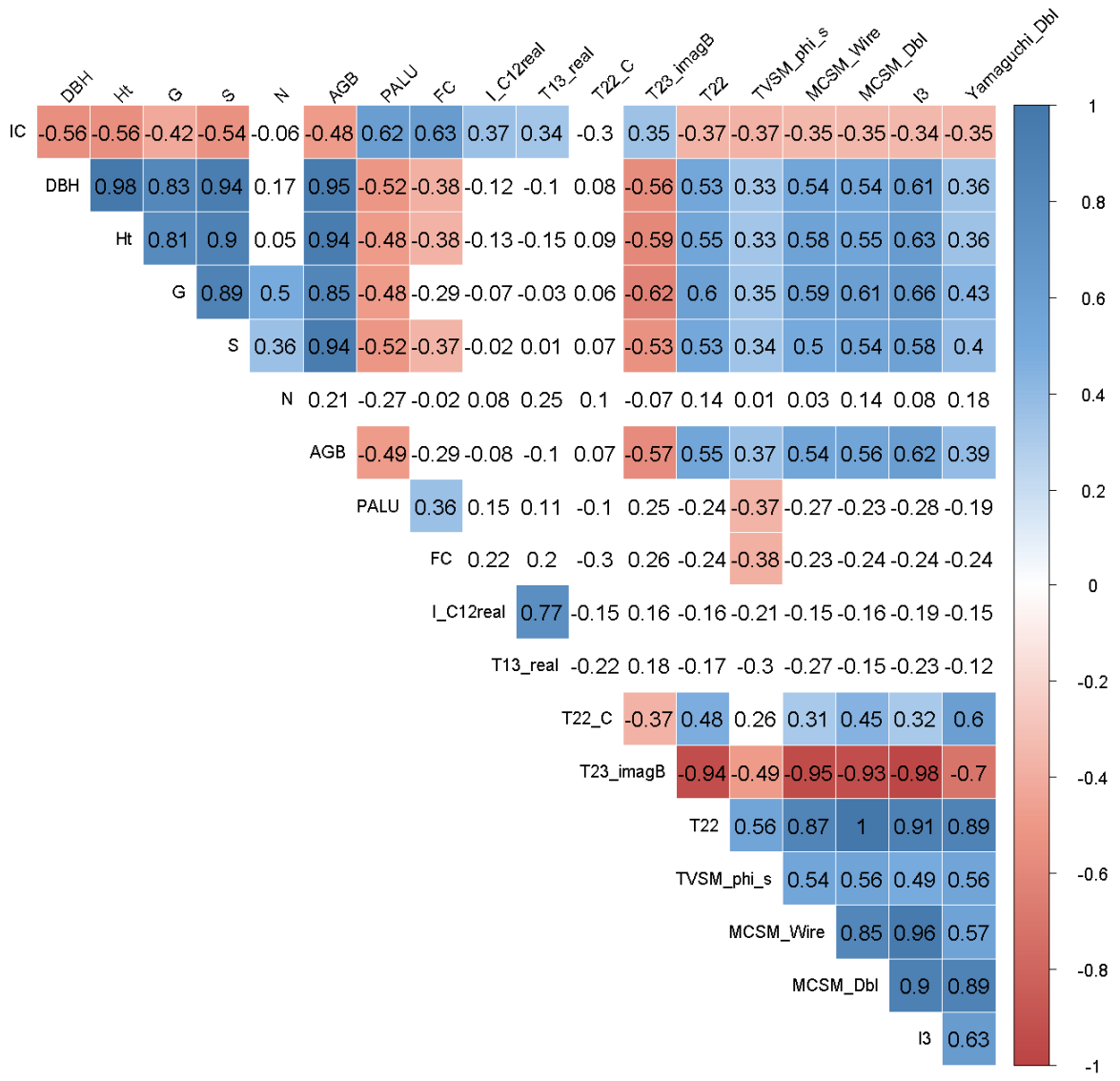

Figure 6. Correlation matrix between biophysical variables and polarimetric parameters for characterization secondary forests by intensity classes. Non-significant values are left blank. Note: IC - Intensity Class of use, DBH - mean diameter at breast height, Ht - mean tree height, G - basal area, S - species density, N - tree density, AGB - aboveground biomass, PALU – period of active land-use, FC - frequency of cuts, I_C12real - real term off diagonal of the covariance matrix $C_{12} = \sqrt{2}\langle S_{HH}S_{HV}^{*}\rangle$, T13_real - real term off diagonal of the coherency matrix $T_{13} = \langle (S_{HH} + S_{VV})S_{HV}^{*}\rangle$, T22_C - relative difference between the co-polarized channels of coherency matrix from Cloude $T_{22}C = \langle |S_{HH} - S_{VV}|^{2}\rangle$, T23_imagB – imaginary term off diagonal of the Barnes-Holm coherency matrix $T_{23}B = \langle (S_{HH} + S_{VV})S_{HV}^{*}\rangle$, T22 - relative difference between the co-polarized channels of coherency matrix $T_{22} = \langle |S_{HH} - S_{VV}|^{2}\rangle$, TVSM_phi_s - Touzi phase module angle, MCSM_Wire - Zhang wire scattering mechanism, MCSM_Dbl - Zhang double-bounce scattering mechanism, I3 - third eigenvalue associated to the respective eigenvector of the Cloude decomposition, and Yamaguchi_Dbl - Yamaguchi double-bounce scattering mechanism.

The Touzi phase module angle $\phi_m = TVSM\_phi\_s$ showed a negative and significant correlation with IC and also a positive and significant correlation with biophysical variables, higher

Preprints (www.preprints.org) | NOT PEER-REVIEWED | Posted: 31 July 2018 doi:10.20944/preprints201807.0604.v1

515 with AGB. On the other hand, the components of the Yamaguchi and Zhang double-bounce
516 scattering mechanism and Zhang's wire scattering component are more strongly correlated with
517 basal area G (ϱ = 0.43, 0.61, 0.59, respectively, p-value <0.005). Areas of SF experiencing greater
518 intensity of use in the past tend to have greater asymmetry of reflection, as shown by the distribution
519 of Touzi phase module angle (ϕ_m) (Figure 7).

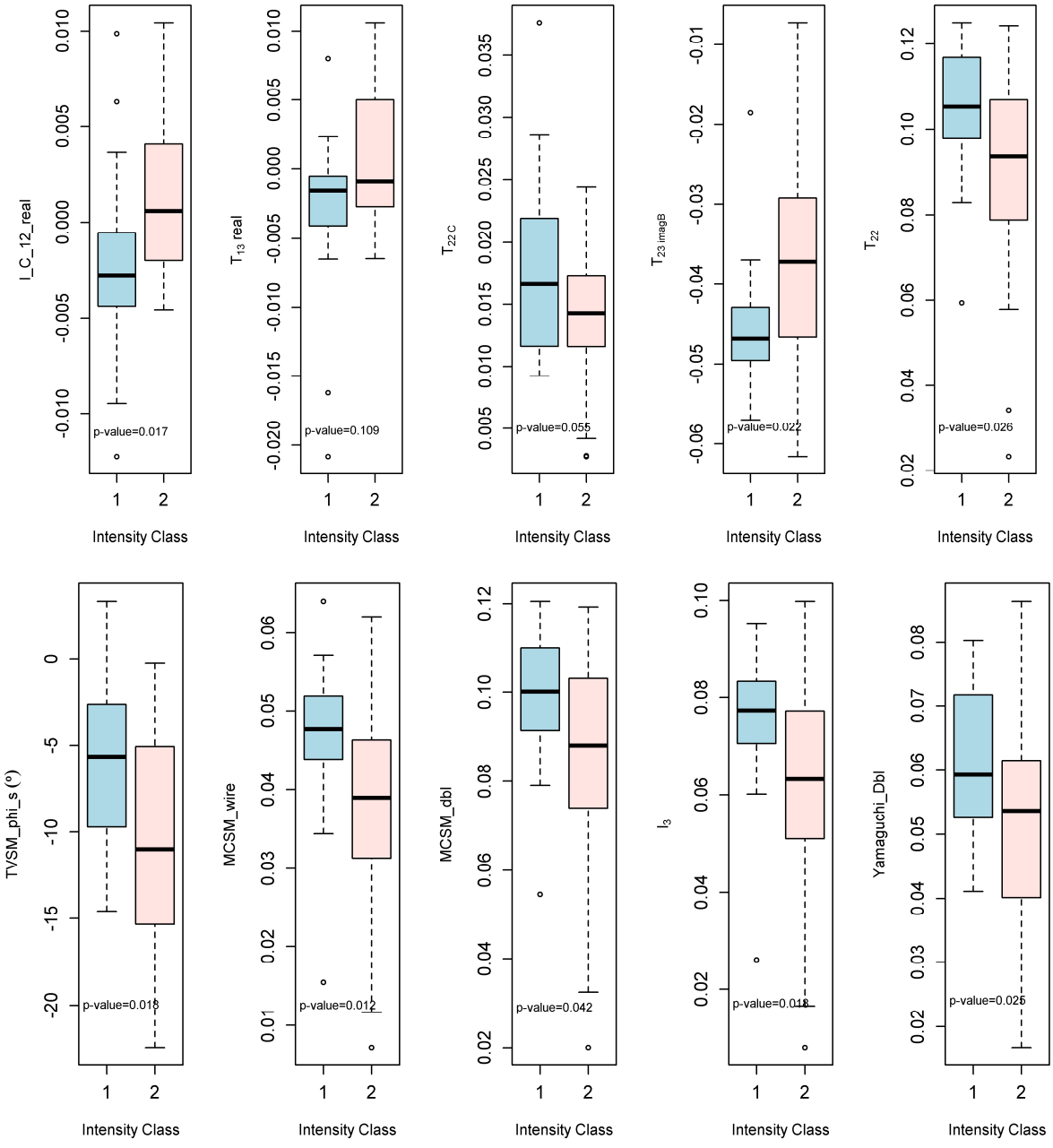

520

521

522 **Figure 7**. Distribution of biophysical variables by intensity class of previous use in the secondary
523 forests of Santarém study using CFS algorithm. I_C12real - real term off diagonal of the covariance
524 matrix $C_{12} = \sqrt{2}\langle S_{HH}S_{HV}^{*}\rangle$, TVSM_phi_s - Touzi phase module angle, MCSM_Dbl - Zhang
525 double-bounce scattering mechanism, MCSM_Wire - Zhang wire scattering mechanism,
526 Yamaguchi_Dbl - Yamaguchi double-bounce scattering mechanism, and l3 = λ_3 - third eigenvalue
527 associated to the respective eigenvector of the Cloude decomposition.

528 *3.4. Modeling AGB*

529 The nonlinear (NL) model using the backscattering coefficient of the cross-polarized channel (σ^0
530 HV) showed signal saturation for AGB values close to 150 Mg ha^{-1} as often reported in the literature
531 (Figure 8).

Preprints (www.preprints.org) | NOT PEER-REVIEWED | Posted: 31 July 2018 doi:10.20944/preprints201807.0604.v1

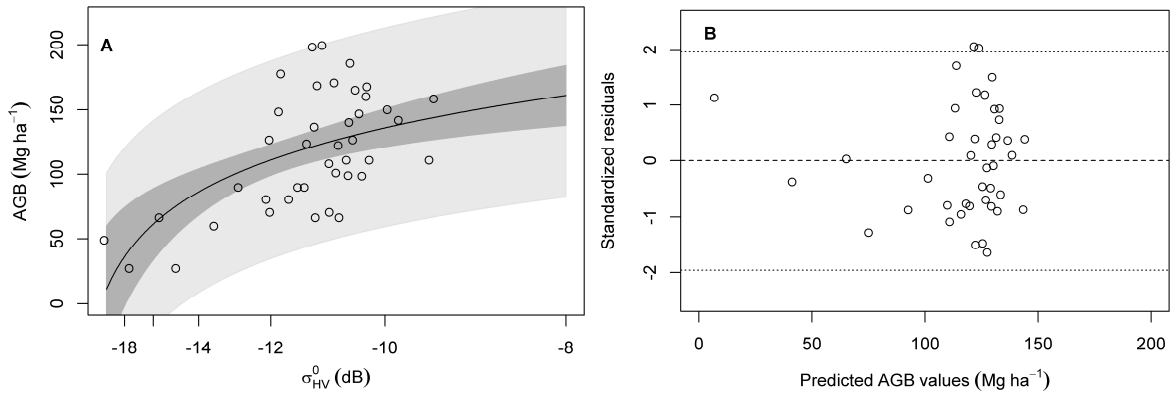

Figure 8. Model performance for the nonlinear regression of AGB as a function of backscattering coefficient σ^0_{HV} in dB. A. Logarithmic fitting to AGB field data. Confidence and prediction intervals shown as dark and light shaded areas respectively. B. Standardized residuals against predicted AGB values.

The fitted NL model has an AIC of 417.1 and R^2 = 0.28 (Table 6). When compared to other studies that used similar models R^2 = 0.44-0.86 [29, 56, 114], we found low R^2 value for the NL model. We argue that this was due to the low amount of data available for the young SF. These young SF usually have higher annual increments of AGB and higher sensitivity to SAR microwave wavelength, before the saturation point than older SFs [17, 31]. The standardized residues, otherwise, were heteroscedastic, rejecting the hypothesis of homoscedasticity of the residuals at the level α = 0.05 (BP: 4.8; p-value <0.05).

Table 6. Model's performance evaluation.

Model	AIC	R^2 validation	RMSE (Mg ha^{-1})	Bias (Mg ha^{-1})
Non linear (NL)	417.1	0.28	12.6	0.3
Multiple Linear Regression (MLR)	408.1	0.37	13.2	2.1
Extended Water Cloud Model (EWCM)	443.0	0.14	15.0	3.4

Using the CFS the algorithm selected nine polarimetric attributes with the highest importance value and ten models by the Akaike criteria Δ AIC < 2 (Figure S.1. Suppl. material). The attributes that presented the highest relative importance in the MLR models were: the real term T_{12} between the channels (HH + VV) and (HH - VV) of the Barnes-Holm decomposition, the ellipticity angles of Neumann (Neumann_tau), and the ellipticity angle of the third component of Touzi (TVSM_tau_s3) (Figure 1).

The attributes of the Touzi decomposition, especially the Touzi magnitude and phase components, are reported to present important information for modeling AGB [29, 56, 82]. Bispo et al. [29] observed a high correlation between AGB and ellipticity angle, but only for the first Touzi component and did not for the third as described here.

Among the ten models pre-selected by the Δ AIC < 2, the best model presented AIC = 407.42 and seven attributes selected, against AIC = 408.13 and AIC = 408.14 for the second and third best models with six and five attributes, respectively. However, the first and third models presented high Variance Inflation Factor (VIF) values for the $\lambda 3$ and T23_imagB attributes, which both have high correlation with AGB indicating multicollinearity problems. So, the best prediction model was the second Eq. (17):

$$BAS\ (Mg.ha^{-1}) = -1151{,}1 + 516{,}6\ (Neumann_{tau}) + 0{,}96\ (TVSM_{tau_{s3}}) + 2809{,}1\ (T23_{imag}) + 592{,}91\ (ES_{P_{norm}}) + 319{,}52\ (ES_{norm}) + 2306{,}73\ (T12_{realB}) \quad (17)$$

Preprints (www.preprints.org) | NOT PEER-REVIEWED | Posted: 31 July 2018 doi:10.20944/preprints201807.0604.v1

The selected model was able to explain slightly more than 50% of the AGB variability in the Santarém's SF ($R^2_{adj.}$ = 0.51), whose parameters were significant at the α = 0.05 level, except for the ellipticity of the third Touzi component and the imaginary component T_{23} of the matrix [T] that were significant at the α = 0.1 level.

Interestingly, the selected polarimetric attributes of the MLR model did not have the highest correlation with the AGB. For instance, the ellipticity of Neumann decomposition has highest and significant correlation with the basal area (G) p-value <0.001 and the normalized Shannon entropy with the mean DBH, p-value = 0.001. These attributes also showed a significant correlation with AGB, Ht, and S at the α = 0.05 level. The third component of Touzi's ellipticity presented higher correlation with the AGB, but it was not significant (p-value> 0.05). The real T_{12} term of the Barnes-Holm decomposition and the imaginary term T23 have a negative correlation with the period of active land-use (PALU), p-value = 0.18 and p-value = 0.42, respectively. The contribution of the degree of depolarization of the normalized Shannon entropy, in turn, showed a higher and not significant correlation with G. The regression residuals present normal distribution (p-value = 0.64) without the presence of possible outliers (Figure S.2. Suppl. material) and absence of homoscedasticity of the residues by the Breusch-Pagan test (BP: 3.46, p-value = 0.063).

The semi-empirical EWCM had the lowest value of Akaike AIC = 395.62 among the three models used in this study, but it stems mainly from the smaller number of training samples used. If the model were made with the total number of samples the AIC value would be approximately AIC = 443 (Table 6). The parameter β calculated for the model was β = 0.00408 ± 0.000454 (p-value <0.001) whose value is similar to β =0.0059 found in the Tropical Forest from India [37]. The residuals of the EWCM model are well homogeneously distributed in the range of BAS = 52.6-180.22 Mg ha^{-1} without the presence of outliers or heteroscedasticity (BP = 0.24; p-value = 0.62) (Figure S.3. Suppl. material). It can be noted that, visually, there is no signal saturation for values of AGB > 150 Mg ha^{-1} (Figure 9E), unlike what happened with the NL model (Figure 9A). Because of this, modifications of the EWCM model have been proposed even in the techniques of PolInSar – Polarimetric Interferometry SAR [35].

The performance of the EWCM was inferior among models, with R^2 = 0.14 and RMSE = 15 ± 8.53 Mg ha^{-1} (Table 6). Bharadwaj et al. [37], on the other hand, observed R^2 = 0.43 for AGB ranging from 10 to 470 Mg ha^{-1} and RMSE = 117.6 Mg ha^{-1} using this model for the estimate of AGB in a Tropical Forest from India. The RMSE from NL model represented about 12% of the mean value of the AGB (RMSE = 12.57 ± 6.66 Mg ha^{-1}). The non-linear model had a bias of the estimate μ_{bias} = 0.26 ± 38.3 Mg ha^{-1} and did not different from zero by the t-test (Figure 9B), besides of the tendency of overestimating the AGB > 100-150 Mg.ha^{-1} (Figure 9A).

The mean error of prediction after cross-validation of MLR was RMSE = 13.19 ± 7.82 Mg ha^{-1} and the AGB prediction showed no clear signal saturation when multiple polarimetric attributes were combined (Figure 9C). However, prediction errors were higher in low AGB values because of multiple interactions between attributes resulted in spurious values resulting from low sampling at AGB values of about 20-70 Mg ha^{-1}. The mean bias error was higher than in the NL model μ_{bias} = 2.1 ± 37.9 Mg ha^{-1} (Figure 9D) and shown not different from zero by the t-test (p-value = 0.1).

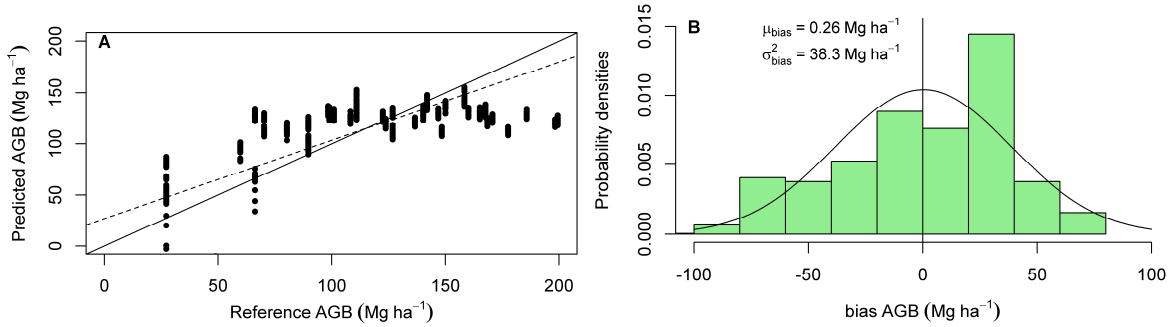

Preprints (www.preprints.org) | NOT PEER-REVIEWED | Posted: 31 July 2018 doi:10.20944/preprints201807.0604.v1

606

607

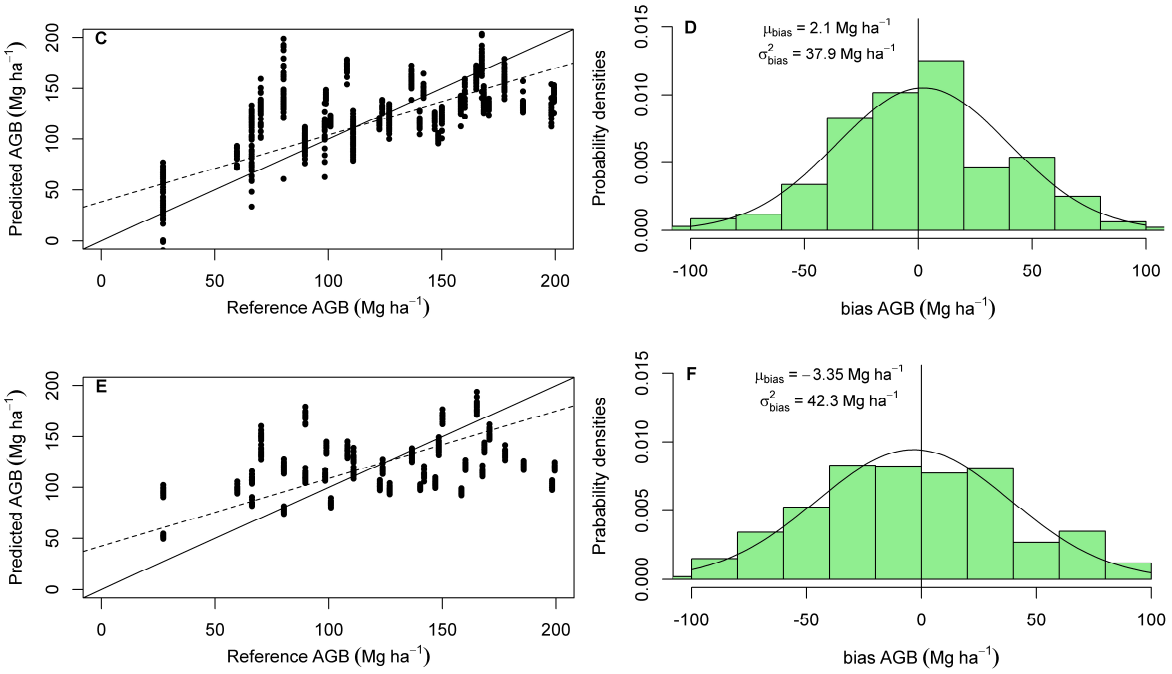

608 **Figure 9**. Bootstrapped cross-validation results for AGB estimation in the secondary forests using
609 non-linear (**A** and **B**), multiple linear (**C** and **D**), and extended water cloud model (**E** and **F**). **A**, **C**, and
610 **E**. Linear regression between reference AGB (x-axis) and predicted AGB (y-axis). The solid line
611 represents the perfect 1: 1 fit and the dotted line the adjustment after cross validation. **B**, **D**, and **F**.
612 Probability density function and histogram of bias of prediction AGB.

613 We observed the saturation signal in our AGB estimate using NL model, as the estimated
614 values AGB are preferably below 100 Mg ha^{-1} (Figure 10A). Using the MLR model (Figure 10B) it is
615 noted that the agricultural areas were classified as NoData (transparent) and a great part of the SF
616 nearby FLONA presents intermediate biomass values AGB = 25-100 Mg ha^{-1}, which are represented
617 by young forests aging less than 16 years. This result is in agreement with the results obtained by
618 Carreiras et al. [20] who observed 57% of SF was aged 6-15 years-old at the same study site. We did
619 not generate a map from EWCM because of the low accuracy of the model.

Preprints (www.preprints.org) | NOT PEER-REVIEWED | Posted: 31 July 2018 doi:10.20944/preprints201807.0604.v1

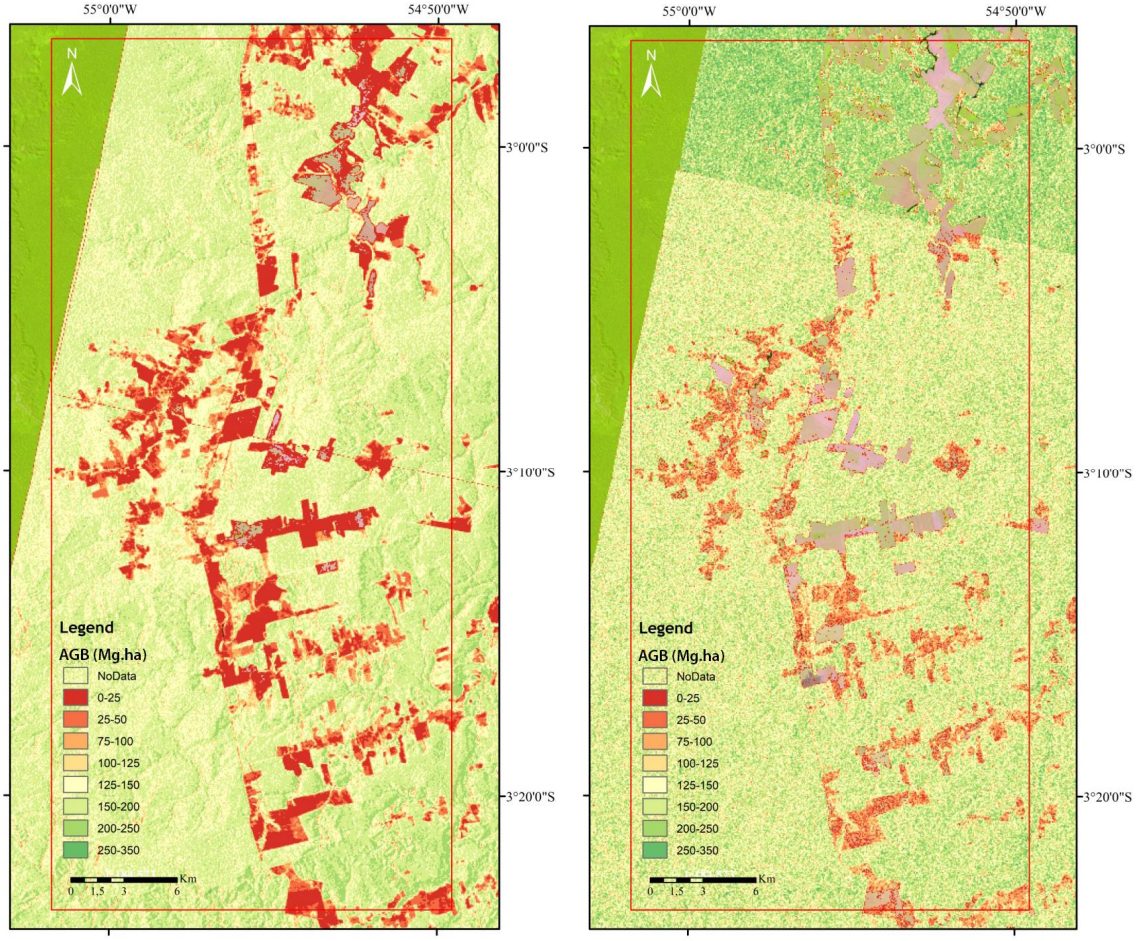

Figure 10. A. Map of above-ground biomass (AGB, Mg ha^{-1}) in the secondary forests of Santarém with the non-linear (NL) model, and B. with multiple linear regression (MLR) model. The background image is Landsat 5 TM false color composite 5-4-3 from 25 Jul 2015.

4. Discussion

4.1. Growth models for biophysical variables

By analyzing the empirical models we showed that biophysical variables had different accumulation rates. While DBH, Ht, G and N could quickly recover during the regrowth of SFs, AGB and S took a much longer time to recover the PFs values. By this reason the classification of the SF in initial, intermediate and advanced succession is often based on structural parameters and not on species richness and composition [12].

Our results demonstrated the patterns of growth for different SF biophysical variables in Santarém. Although the graphs showed the growth curves up to a 40 year interval, the input data included SFs younger than 30 years-old. This was the reason why the growth models tested could not be fitted without the asymptote being fixed – 2nd model assumptions [17]. The age distribution of plots (up to 28 years) is quite narrow as the most pioneer species ages (48-162), so this approach might be less useful at more advanced stages of secondary succession [2, 104].

Growth curves of AGB attained asymptotic values at more than 100 years. These reports do not match observations made by Neeff and Santos [17], who found out the asymptote in the 40-50 years of young SFs in the Santarém site. However, they used power model for modeling AGB growth and fixed the maximum AGB values of 192.8 Mg ha^{-1} of the mature forest. Others authors depicted similar accumulation of biomass in young SF up to 100 Mg ha^{-1} at less than 15 years [2]. Houghton et al. [105] considered a superior AGB accumulation in their model at age 25, with almost 70% of AGB from PF. The Houghton's model was obtained by the product of the growth rate estimated by Brown

and Lugo [2] MAI = 11 Mg ha^{-1} yr^{-1} for SF < 10 years in the entire Brazilian Amazon, regardless of the land-use history [2]. Our value of MAI is almost 2.5 times higher than the 1.5 Mg C ha^{-1} yr^{-1} estimated by Houghton et al. [105] for SFs with AGB < 100 Mg ha^{-1} used in the model of annual carbon flux from regeneration areas in the Brazilian Amazon. We argue the absence of emergent slow growth species that have the largest contribution to AGB [53] as a possible cause for reducing the rates of recovery of AGB in our study.

These growth models are not only applicable for estimating biophysical variables of the SFs using ALOS-2 PALSAR-2 data, but also for carbon budget estimation and ecological application. The chronosequences of SFs were obtained in areas that suffered distinct previous intensity of use and despite neglecting them in growth models it is rely on assumptions relating to the ecological process of the forest growth.

The results indicate that the SF monitoring in the tropics should cover a broader range of ages, specifically including SFs older than 100 years. The widening of the age spectrum would allow an increase in accuracy of growth models due to a better characterization of the underlying sources of variation, such as the intensity of previous use, the soil characteristics, among others. These long-term surveys could be useful to confirm the hypothesis of the different degrees of SF resilience across the Amazon Basin [106, 107].

4.2. Polarimetric data for SF characterization

The polarimetric attributes extracted from the ALOS-2 PALSAR-2 data allowed to separate the SF by their ICs, but the p-values were close to the critical value of H_0 (α = 0.05). One reason may be the low sampling in the initial secondary succession stages where the backscattering saturation is not close as the saturation point [108]. Other possible reason could be the attenuation caused by the growth models which did not encompasses previous uses, smoothing structural differences in forest parameters related to intensity before abandonment. It is known that areas of SFs had significant differences according to their past use. For instance, the increment of the AGB in areas previously burned 4-5 times can be 50% less than in the areas abandonment right after clear-cut [27]. Uhl et al. [66] reported a strong reduction in biomass accumulation at 8 years of the SF in the Central Amazon. The AGB was 60-87 Mg ha^{-1} after one year of grazing, 28 Mg ha^{-1} with 6 years of grazing and only 0.16 Mg ha^{-1} with 11 years of grazing. This slow increment related to past use was significant up to 18 years-old, but disappear at advanced secondary succession stages [28]. Such differences on structural parameters of the SFs could highlight the divergences among polarimetric attributes by intensity classes.

One of the best attribute, C_{12real}, showed p-value = 0.017 for ICs separation, and low complex coherence of lighter use class. Probably the more complex structure of SF with lower past intensity use (IC =1) could be producing depolarization between the HH and HV channels when compared to SF with higher intensity use (IC = 2). The hypothesis that forested areas show reflection symmetry can be denied by the value of C_{12real}, since according to Lee and Pottier [104], the elements outside the main diagonal of the covariance matrix are null if they satisfy the condition of reflection symmetry (monostatic case). This observation motivated us to apply the non usual terms off diagonal of coherence and covariance matrices as a prediction variables, despite of their physical relationship with forest targets is not fully understood.

4.3. Regression models

Our results showed good performance of the regression models varying from R^2 = 0.14 to 0.51 (Table 4). The best model performance was the MLR and the lowest the EWCM. In the selected MLR model it was observed the importance of polarimetric attributes not commonly used for AGB estimation as the terms off diagonal of the coherency and covariance matrices. The importance of these attributes have been neglected from analysis in the literature by believe they were null under reflection symmetry assumption. And instead of being related to AGB, they were correlated to other biophysical parameters such as the N, G, and average DBH, which in turn are related to the previous land-use. Furthermore, recent polarimetric decompositions approaches as Shannon Entropy and

Neumann also presented good relationships with AGB and can be useful for other forest applications [128, 118].

Although EWCM has had the least performance, it has a potential to be used due to physical meaning of β parameter which has a linear relation with biomass amount. Moreover, the EWCM model showed to be independent of forest area or location, and does not presenting signal saturation for higher AGB values [37]. The EWCM is based on the interaction of the contribution of the three main scattering mechanisms with AGB, and can be modeled by only one parameter β. However, the EWCM is highly sensitive to outliers [35, 37], and the preprocessing tests should be made in order to avoid mean shift in the orientation angle in the analysis. The de-orientation of the targets is caused by the change in the angle of orientation with respect to the line of sight of the sensor, as result of the azimuth and slope of the relief. The direct effect of the de-orientation is the rotation of [T] and, consequently, the increase of the volumetric scattering and decrease of the double-bounce and superficial scatters [35]. We also proved that reflection symmetry is unsolved and showed how it affects the polarimetric decomposition assumptions and their relation to biophysical variables. Although estimated β parameter has had realistic number, the small numbers of younger SF (age < 7 years) could have underestimated this forest parameter. It is recommended, however, to perform the de-orientation correction of the coherence matrix [T] before the modeling to reduce the number of outliers and increase the accuracy of the AGB estimation.

4.4. Uncertainty report

Several sources of uncertainty could be identified which are mainly originated by the propagation of errors from the field data to remote sensing analysis. These errors included inherent inventory errors, the choice of the hypsometric equation for height estimation, the allometric equation for the AGB estimation, and the expansion errors of individual trees for the plot analysis. In addition, the errors related to the growth modeling and from the land-use history, the errors of the geometric co-registration and orthorectification, the inherent errors of the sensor instrument and, finally, the errors from regression models.

The inventory errors were set up at 10%, the error of the allometric equation was RMSE = 14%, and the errors of individual tree expansion for plot analysis was RMSE = 49%. The errors of AGB growth models were RMSE = 5.4% and the ones from the history of use were on average 17% [20]. Inherent sensor instrument errors include speckle noise, calibration errors, topographic effects and variability sources as moisture content, but they were not computed here. The value modeled by the sum of these components calculated by Ahmed et al. [109] was $\sigma^{\circ} = 0.025$ dB, that is, less than 2% of the mean backscatter coefficient of the SF. Co-registration errors were not computed, but were smoothed due to the use of the mean of the attributes in each plot. The errors from MLR model were RMSE = 8.92%.

The error propagation was not modeled, but a good approximation can be made computing the mean errors, considering that they are independent and not correlated with each other [110]. In such case, the mean error of AGB estimation was greater than 15% considering all the mentioned sources of uncertainty. It is noted that the errors related to the choice of the allometric equation for the individual biomass estimation and to the expansion of the individual tree analysis for the plot analysis represent more than 50% of the total errors in Santarém site. The smallest errors come from SAR data and processing, as well as from the regression models, which were less than 20% of the average total errors.

5. Conclusions

The main goal of this research was to estimate the aboveground biomass (AGB) in the Secondary Forest (SF) from Santarém site using the polarimetric ALOS-2 PALSAR-2 data. The Chapman-Richards models were used to update the biophysical variables to PALSAR-2 acquisition date time. The CR growth models showed that mean diameter (DBH), mean tree height (Ht), and basal area (G) had highest increment among biophysical variables reaching half of asymptote in less

than 15 years on SFs. However, the AGB and the number of species per hectare (S) may reach half of asymptote after 25 years, and 90% of asymptote beyond 100 years.

We also used polarimetric data to characterize the SFs by previous land use intensity, and the data from SF plots was splitted into two intensity classes (IC) of use: 1- light use (after the clear cut and inferior of 2 years of use) and 2 - moderate to heavy use (after a period of more than two years of use before abandonment or two or more cuts in the same area. The ICs presented significant floristic and structural differences regarding the previous intensity of use. For instance, IC = 1 showed greater DBH, Ht, G, S, and AGB in the SF for ($p < 0.05$), but not for number of individuals per hectare ($p = 0.72$).

Such differences in the previous land-use were observed using polarimetric attributes with emphasis on the real component of the covariance matrix between the channels HH and HV (C_{12real}) the Touzi phase module angle (TVSM_phis_s), the second diagonal component of the Cloude coherence matrix. (T_{22_C}), and the double-bounce scattering mechanism from Yamaguchi and Zhang decomposition.

Among the models tested, the multiple linear regression (MLR) model presented the best performance $R^2 = 0.51$, RMSE = 13.19 Mg ha^{-1} (8.9%). It improves up to 70% of the model performance comparing with non linear model. The polarimetric attributes of the MLR model were strongest related with different structural parameters such as DBH, G, and Ht, instead of AGB. The uncertainties of the MLR were estimated to be less than 15%.

Acknowledgments: The authors are grateful to the Coordenação de Aperfeiçoamento de Pessoal de Nível Superior (CAPES), the Conselho Nacional de Desenvolvimento Científico e Tecnológico (CNPq), the Instituto Nacional de Pesquisas Espaciais (INPE), the REGROWTH-BR Project, and the G-FOI project. Thanks are also for the botanical assistance Chico, Graveto, and Letícia and Large Scale Biosphere-Atmosphere Experiment in Amazonia (LBA-Santarém Office) for the logistic support during the field surveys. We thanks to JAXA and the Kyoto & Carbon Initiative for providing ALOS-2 PALSAR-2 data. J.M.B.C. was funded as part of NERC's support of the National Centre for Earth Observation

Author Contributions: H.L.G.C. developed the research, conceived, designed the experiments, and also analyzed the data and wrote the article. Y.E.S and E.C.M supervised all stages of the research as advisors and also comments. J.M.B.C. provided the ALOS-2 data, contributed for methodological and discussion analysis, L.E.O.C.A. contributed to editing, revision and discussion of the paper. C.V.J.S. provided field sample data of young secondary forest and helped with revision manuscript. S.Q. contributed to editing and discussion.

Conflicts of Interest: "The authors declare no conflict of interest." "The founding sponsors had no role in the design of the study; in the collection, analyses, or interpretation of data; in the writing of the manuscript, and in the decision to publish the results".

Appendix A

Table A.1. Polarimetric attributes

Input Matrix	Nº Attr.	Polarimetric Attributes	Reference
C3	9	I_C11, I_C12imag, I_C12real, I_C13imag, I_C13real, I_C22, I_C23imag, I_C23real, I_C33	[111]
C3	3	Freeman_Dbl, Freeman_Odd, Freeman_Vol	[117]
C3	2	$\varrho_{hh\text{-}vv}$, $\lvert\varrho_{hh\text{-}vv}\rvert$	[111]
C3	3	Neumann_mDelta, Neumann_phDelta, Neumann_tau	[118]
C3	3	VanZyl_Dbl, VanZyl_Odd, VanZyl_Vol	[119]
C3	4	Yamaguchi_Dbl, Yamaguchi_Hlx, Yamaguchi_Odd, Yamaguchi_Vol	[120]
C3	4	Bhattacharya_Dbl, Bhattacharya_Hlx, Bhattacharya_Odd, Bhattacharya_Vol	[121]
C3	5	MCSM_Dbl, MCSM_DblHlx, MCSM_Odd, MCSM_Vol, MCSM_Wire	[113]
C3	4	Singh_Dbl, Singh_Hlx, Singh_Odd, Singh_Vol	[122]
S, T3	16	TSVM_alpha_s, TSVM_alpha_s1, TSVM_alpha_s2, TSVM_alpha_s3, TSVM_phi_s, TSVM_phi_s1, TSVM_phi_s2, TSVM_phi_s3, TSVM_psi_s, TSVM_psi_s1, TSVM_psi_s2, TSVM_psi_s3, TSVM_tau_s, TSVM_tau_s1, TSVM_tau_s2, TSVM_tau_s3	[123]

Preprints (www.preprints.org) | NOT PEER-REVIEWED | Posted: 31 July 2018 doi:10.20944/preprints201807.0604.v1

T3	9	T11,T12imag,T12real,T13imag,T13real,T22,T23imag,T23real,T33	[111]
T3	15	A, H, α, β, λ, γ, δ, p_1, p_2, p_3, HA, H_A, λ_1,λ_2,λ_3	[124]
T3	9	T11_H,T12imag_H,T12real_H,T13imag_H,T13real_H,T22_H,T23imag_H,T23real_H,T33_H	[125]
T3	9	T11_C,T12imag_C,T12real_C,T13imag_C,T13real_C,T22_C,T23imag_C,T23real_C,T33_C	[126]
T3	9	T11_B,T12imag_B,T12real_B,T13imag_B,T13real_B,T22_B,T23imag_B,T23real_B,T33_B	[127]
T3	6	ES, ES_norm, ES_I, ES_I_norm, ES_P, ES_P_norm	[128]
T3	4	SERD, SERD_norm, DERD, DERD_norm	[129]
T3	1	PH - pedestal height	[130]
T3	1	PF - polarisation fraction	[131]
T3	1	RVI - radar vegetation index	[119]
C3	3	VSI – vegetation scattering index, BMI – biomass index, CSI – canopy structure index	[132]
C3	1	RFDI – radar forest degradation index	[133]
C3	1	Span (Total Power)	[111]
C3	2	Rpp – parallel polarization ratio, Rcp – cross-polarization ratio	[134]
C3	1	Forest	[38]

Note: C3 - covariance 3 x 3 matrix, T3 - coherency 3 x 3 matrix, S - Sinclair 2 x 2 matrix, ϱhh-vv - modulus of the complex coherency between hh-vv linear polarizations, |ϱhh-vv| - magnitude of the complex coherency between hh-vv linear polarizations, MCSM - Multiple-Component Scattering Model, TSVM - Target Scattering Vector Model, ES - entropy Shannon, SERD – Double-bounce Eigenvalue Relative Difference, DERD – Single-bounce Eigenvalue Relative Difference. **Notation**: *Xnm*_imag imaginary part of *nm* term of x matrix, *Xnm*_real real part of *nm* term of *x* matrix, *Z_Dbl* double-bounce scattering mechanism from the *Z* decomposition, *Z_Vol* volumetric scattering form the *Z* decomposition, *Z_Odd* odd-bounce scattering mechanism form *Z* decomposition, *Z_Hlx* helix scattering mechanism from *Z* decomposition, *Z_Wire* wire scattering mechanism from *Z* decomposition,

References

1. CDB 2014. Definitions: Indicative definitions taken from the Report of the ad hoc technical expert group on forest biological diversity. Available online: https://www.cbd.int/forest/definitions.shtml (accessed on 18 Sep 2014).
2. Brown, S.; Lugo, A. E. Tropical secondary forests. *J. Trop. Ecol.* **1990**, 6, 1–32, doi:10.1017/S0266467400003989.
3. Corlett, R. T. What is Secondary Forest? *J. Trop. Ecol.* **1994**, 10, 445–447.
4. Whitmore, T. C. *An Introduction to Tropical Rainforests*, 2nd ed.; Oxford University Press: New York, USA, 1998; ISBN 9780198501473.
5. FAO 2003. Workshop on Tropical Secondary Forest Management in Africa: Reality and Perspectives. Available online: http://www.fao.org/docrep/006/j0628e/J0628E10.htm#P572_41806 (accessed on 15 May 2014).
6. FAO 2001. Global Forest Resources Assessment 2000. FAO Forestry Paper, n. 140. Roma: Main Report. 511p. Available online: http://www.fao.org/forestry/fra/fra2010/en/ (accessed on 10 Sep 2014).
7. FAO 2010. Global Forest Resources Assessment 2010. FAO Forestry Paper, n. 163. Roma: Main Report. 373p. Available online: http://www.fao.org/forestry/fra/86624/en/ (accessed on 10 Sep 2014).
8. Achard, F. Determination of Deforestation Rates of the World's Humid Tropical Forests. *Science (80-.).* **2002**, *297*, 999–1002, doi:10.1126/science.1070656.
9. Chazdon, R. L. Tropical forest recovery: legacies of human impact and natural disturbances. *Perspect. Plant Ecol. Evol. Syst.* **2003**, *6*, 51–71, doi:10.1078/1433-8319-00042.
10. Pan, Y.; Birdsey, R. A.; Fang, J.; Houghton, R.; Kauppi, P. E.; Kurz, W. A.; Phillips, O. L.; Shvidenko, A.; Lewis, S. L.; Canadell, J. G.; Ciais, P.; Jackson, R. B.; Pacala, S. W.; McGuire, A. D.; Piao, S.; Rautiainen, A.; Sitch, S.; Hayes, D. A Large and Persistent Carbon Sink in the World's Forests. *Science (80-.).* **2011**, *333*, 988–993, doi:10.1126/science.1201609.

11. Gibson, L.; Lee, T. M.; Koh, L. P.; Brook, B. W.; Gardner, T. A.; Barlow, J.; Peres, C. A.; Bradshaw, C. J. A.; Laurance, W. F.; Lovejoy, T. E.; Sodhi, N. S. Erratum: Corrigendum: Primary forests are irreplaceable for sustaining tropical biodiversity. *Nature* **2014**, *505*, 710–710, doi:10.1038/nature12933.
12. Chazdon, R. L. *Second Growth*: The promise of Tropical Forest Regeneration in an Age of Deforestation. Chicago: Chicago Press, 2014.
13. Harris, N. L.; Brown, S.; Hagen, S. C.; Saatchi, S. S.; Petrova, S.; Salas, W.; Hansen, M. C.; Potapov, P. V.; Lotsch, A. Baseline Map of Carbon Emissions from Deforestation in Tropical Regions. *Science (80-.).* **2012**, *336*, 1573–1576, doi:10.1126/science.1217962.
14. Chazdon, R. L.; Broadbent, E. N.; Rozendaal, D. M. A.; Bongers, F.; Zambrano, A. M. A.; Aide, T. M.; Balvanera, P.; Becknell, J. M.; Boukili, V.; Brancalion, P. H. S.; Craven, D.; Almeida-Cortez, J. S.; Cabral, G. A. L.; de Jong, B.; Denslow, J. S.; Dent, D. H.; DeWalt, S. J.; Dupuy, J. M.; Duran, S. M.; Espirito-Santo, M. M.; Fandino, M. C.; Cesar, R. G.; Hall, J. S.; Hernandez-Stefanoni, J. L.; Jakovac, C. C.; Junqueira, A. B.; Kennard, D.; Letcher, S. G.; Lohbeck, M.; Martinez-Ramos, M.; Massoca, P.; Meave, J. A.; Mesquita, R.; Mora, F.; Munoz, R.; Muscarella, R.; Nunes, Y. R. F.; Ochoa-Gaona, S.; Orihuela-Belmonte, E.; Pena-Claros, M.; Perez-Garcia, E. A.; Piotto, D.; Powers, J. S.; Rodriguez-Velazquez, J.; Romero-Perez, I. E.; Ruiz, J.; Saldarriaga, J. G.; Sanchez-Azofeifa, A.; Schwartz, N. B.; Steininger, M. K.; Swenson, N. G.; Uriarte, M.; van Breugel, M.; van der Wal, H.; Veloso, M. D. M.; Vester, H.; Vieira, I. C. G.; Bentos, T. V.; Williamson, G. B.; Poorter, L. Carbon sequestration potential of second-growth forest regeneration in the Latin American tropics. *Sci. Adv.* **2016**, *2*, e1501639–e1501639, doi:10.1126/sciadv.1501639.
15. Aragão, L. E. O. C.; Poulter, B.; Barlow, J. B.; Anderson, L. O.; Malhi, Y.; Saatchi, S.; Phillips, O. L.; Gloor, E. Environmental change and the carbon balance of Amazonian forests. *Biol. Rev.* **2014**, *89*, 913–931, doi:10.1111/brv.12088.
16. Houghton, R. A.; Skole, D. L.; Nobre, C. A.; Hackler, J. L.; Lawrence, K. T.; Chomentowski, W. H. Annual fluxes of carbon from deforestation and regrowth in the Brazilian Amazon. *Nature* **2000**, *403*, 301–304, doi:10.1038/35002062.
17. Neeff, T.; Santos, J. R. dos A growth model for secondary forest in Central Amazonia. *For. Ecol. Manage.* **2005**, *216*, 270–282, doi:10.1016/j.foreco.2005.05.039.
18. Wandelli, E. V.; Fearnside, P. M. Secondary vegetation in central Amazonia: Land-use history effects on aboveground biomass. *For. Ecol. Manage.* **2015**, *347*, 140–148, doi:10.1016/j.foreco.2015.03.020.
19. Carreiras, J. M. B.; Pereira, J. M. C.; Campagnolo, M. L.; Shimabukuro, Y. E. Assessing the extent of agriculture/pasture and secondary succession forest in the Brazilian Legal Amazon using SPOT VEGETATION data. *Remote Sens. Environ.* **2006**, *101*, 283–298, doi:10.1016/j.rse.2005.12.017.
20. Carreiras, J. M. B.; Jones, J.; Lucas, R. M.; Gabriel, C. Land Use and Land Cover Change Dynamics across the Brazilian Amazon: Insights from Extensive Time-Series Analysis of Remote Sensing Data. *PLoS One* **2014**, *9*, e104144, doi:10.1371/journal.pone.0104144.
21. Almeida, C. A.; Valeriano, D. M.; Escada, M. I. S.; Rennó, C. D. Estimativa de área de vegetação secundária na Amazônia Legal Brasileira. *Acta Amaz.* **2010**, *40*, 289–301, doi:10.1590/S0044-59672010000200007.
22. INPE 2010. Projeto Terra Class: Levantamento de informações de uso e cobertura da terra na Amazônia. Available online: http://www.inpe.br/cra/projetos_pesquisas/terraclass2010.php. (accessed on 20 Sep 2014).
23. INPE 2014. Projeto PRODES: Monitoramento da Floresta Amazônica Brasileira por Satélite. Available online: http://www.obt.inpe.br/prodes/index.php. (accessed on 20 Sep 2014).
24. Lucas, R. M.; Xiao, X.; Hagen, S.; Frolking, S. Evaluating TERRA-1 MODIS data for discrimination of tropical secondary forest regeneration stages in the Brazilian Legal Amazon. *Geophys. Res. Lett.* **2002**, *29*, 42-1-42–4, doi:10.1029/2001GL013375.
25. Asner, G. P.; Rudel, T. K.; Aide, T. M.; Defries, R.; Emerson, R. A Contemporary Assessment of Change in Humid Tropical Forests. *Conserv. Biol.* **2009**, *23*, 1386–1395, doi:10.1111/j.1523-1739.2009.01333.x.
26. Lucas, R. M.; Honzák, M.; Amaral, I. Do; Curran, P. J.; Foody, G. M. Forest regeneration on abandoned clearances in central Amazonia. *Int. J. Remote Sens.* **2002**, *23*, 965–988, doi:10.1080/01431160110069791.
27. Zarin, D. J.; Davidson, E. a; Brondizio, E.; Vieira, I. C. G.; Sá, T.; Schuur, E. a G.; Mesquita, R.; Moran, E.; Delamonica, P.; Mark, J.; Hurtt, G. C.; Salimon, C.; Denich, M. Legacy of fire slows carbon

accumulation in. *Ecology* **2005**, *3*, 365–369, doi:10.1890/1540-9295(2005)003%5B0365:LOFSCA%5D2.0.CO;2.

28. Bonner, M. T. L.; Schmidt, S.; Shoo, L. P. A meta-analytical global comparison of aboveground biomass accumulation between tropical secondary forests and monoculture plantations. *For. Ecol. Manage.* **2013**, *291*, 73–86, doi:10.1016/j.foreco.2012.11.024.
29. Bispo, P. C.; Santos, J. R.; Valeriano, M. M.; Touzi, R.; Seifert, F. M. Integration of Polarimetric PALSAR Attributes and Local Geomorphometric Variables Derived from SRTM for Forest Biomass Modeling in Central Amazonia. *Can. J. Remote Sens.* **2014**, *40*, 26–42, doi:10.1080/07038992.2014.913477.
30. Vafaei, S.; Soosani, J.; Adeli, K.; Fadaei, H.; Naghavi, H.; Pham, T.; Tien Bui, D. Improving Accuracy Estimation of Forest Aboveground Biomass Based on Incorporation of ALOS-2 PALSAR-2 and Sentinel-2A Imagery and Machine Learning: A Case Study of the Hyrcanian Forest Area (Iran). *Remote Sens.* **2018**, *10*, 172, doi:10.3390/rs10020172.
31. Saatchi, S.; Halligan, K.; Despain, D. G.; Crabtree, R. L. Estimation of Forest Fuel Load From Radar Remote Sensing. *IEEE Trans. Geosci. Remote Sens.* **2007**, *45*, 1726–1740, doi:10.1109/TGRS.2006.887002.
32. Ghasemi, N.; Sahebi, M. R.; Mohammadzadeh, A. Biomass estimation of a temperate deciduous forest using wavelet analysis. *IEEE Trans. Geosci. Remote Sens.* **2013**, *51*, 765–776, doi:10.1109/TGRS.2012.2205260.
33. Avtar, R.; Suzuki, R.; Sawada, H. Natural Forest Biomass Estimation Based on Plantation Information Using PALSAR Data. *PLoS One* **2014**, *9*, e86121, doi:10.1371/journal.pone.0086121.
34. Vaglio Laurin, G.; Pirotti, F.; Callegari, M.; Chen, Q.; Cuozzo, G.; Lingua, E.; Notarnicola, C.; Papale, D. Potential of ALOS2 and NDVI to Estimate Forest Above-Ground Biomass, and Comparison with Lidar-Derived Estimates. *Remote Sens.* **2016**, *9*, 18, doi:10.3390/rs9010018.
35. Kumar, S.; Pandey, U.; Kushwaha, S. P.; Chatterjee, R. S.; Bijker, W. Aboveground biomass estimation of tropical forest from Envisat advanced synthetic aperture radar data using modeling approach. *J. Appl. Remote Sens.* **2012**, *6*, 063588, doi:10.1117/1.JRS.6.063588.
36. Attema, E. P. W.; Ulaby, F. T. Vegetation modeled as a water cloud. *Radio Sci.* **1978**, *13*, 357–364, doi:10.1029/RS013i002p00357.
37. Sai Bharadwaj, P.; Kumar, S.; Kushwaha, S. P. S.; Bijker, W. Polarimetric scattering model for estimation of above ground biomass of multilayer vegetation using ALOS-PALSAR quad-pol data. *Phys. Chem. Earth, Parts A/B/C* **2015**, *83–84*, 187–195, doi:10.1016/j.pce.2015.09.003.
38. Viet Nguyen, L.; Tateishi, R.; Thanh Nguyen, H.; C. Sharma, R.; Trong To, T.; Mai Le, S. Estimation of Tropical Forest Structural Characteristics Using ALOS-2 SAR Data. *Adv. Remote Sens.* **2016**, *05*, 131–144, doi:10.4236/ars.2016.52011.
39. Scatena, F. N.; Walker, R. T.; Homma, A. K. O.; de Conto, A. J.; Ferreira, C. A. P.; de Amorim Carvalho, R.; da Rocha, A. C. P. N.; dos Santos, A. I. M.; de Oliveira, P. M. Cropping and fallowing sequences of small farms in the "terra firme" landscape of the Brazilian Amazon: a case study from Santarem, Para. *Ecol. Econ.* **1996**, *18*, 29–40, doi:10.1016/0921-8009(95)00055-0.
40. Roosevelt, A. C.; Housley, R. A.; Da Silveira, M. I.; Maranca, S.; Johnson, R. Eighth Millennium Pottery from a Prehistoric Shell Midden in the Brazilian Amazon. *Science (80-.).* **1991**, *254*, 1621–1624, doi:10.1126/science.254.5038.1621.
41. Fearnside, P. M. Deforestation in Brazilian Amazonia: History, Rates, and Consequences. *Conserv. Biol.* **2005**, *19*, 680–688, doi:10.1111/j.1523-1739.2005.00697.x.
42. Aragão, L. E. O. C.; Anderson, L. O.; Fonseca, M. G.; Rosan, T. M.; Vedovato, L. B.; Wagner, F. H.; Silva, C. V. J.; Silva Junior, C. H. L.; Arai, E.; Aguiar, A. P.; Barlow, J.; Berenguer, E.; Deeter, M. N.; Domingues, L. G.; Gatti, L.; Gloor, M.; Malhi, Y.; Marengo, J. A.; Miller, J. B.; Phillips, O. L.; Saatchi, S. 21st Century drought-related fires counteract the decline of Amazon deforestation carbon emissions. *Nat. Commun.* **2018**, *9*, 536, doi:10.1038/s41467-017-02771-y.
43. Gonçalves, F. G.; Santos, J. R. dos Composição florística e estrutura de uma unidade de manejo florestal sustentável na Floresta Nacional do Tapajós, Pará. *Acta Amaz.* **2008**, *38*, 229–244, doi:10.1590/S0044-59672008000200006.
44. Vieira, S.; de Camargo, P. B.; Selhorst, D.; da Silva, R.; Hutyra, L.; Chambers, J. Q.; Brown, I. F.; Higuchi, N.; dos Santos, J.; Wofsy, S. C.; Trumbore, S. E.; Martinelli, L. A. Forest structure and carbon dynamics in Amazonian tropical rain forests. *Oecologia* **2004**, *140*, 468–479, doi:10.1007/s00442-004-1598-z.

45. Quesada, C. A.; Lloyd, J.; Schwarz, M.; Patiño, S.; Baker, T. R.; Czimczik, C.; Fyllas, N. M.; Martinelli, L.; Nardoto, G. B.; Schmerler, J.; Santos, A. J. B.; Hodnett, M. G.; Herrera, R.; Luizão, F. J.; Arneth, A.; Lloyd, G.; Dezzeo, N.; Hilke, I.; Kuhlmann, I.; Raessler, M.; Brand, W. A.; Geilmann, H.; Moraes Filho, J. O.; Carvalho, F. P.; Araujo Filho, R. N.; Chaves, J. E.; Cruz Junior, O. F.; Pimentel, T. P.; Paiva, R. Variations in chemical and physical properties of Amazon forest soils in relation to their genesis. *Biogeosciences* **2010**, *7*, 1515–1541, doi:10.5194/bg-7-1515-2010.
46. Silver, W. L.; Neff, J.; McGroddy, M.; Veldkamp, E.; Keller, M.; Cosme, R. Effects of Soil Texture on Belowground Carbon and Nutrient Storage in a Lowland Amazonian Forest Ecosystem. *Ecosystems* **2000**, *3*, 193–209, doi:10.1007/s100210000019.
47. Telles, E. de C. C.; de Camargo, P. B.; Martinelli, L. A.; Trumbore, S. E.; da Costa, E. S.; Santos, J.; Higuchi, N.; Oliveira, R. C. Influence of soil texture on carbon dynamics and storage potential in tropical forest soils of Amazonia. *Global Biogeochem. Cycles* **2003**, *17*, n/a-n/a, doi:10.1029/2002GB001953.
48. Lu, D.; Moran, E.; Mausel, P. Linking Amazonian secondary succession forest growth to soil properties. *L. Degrad. Dev.* **2002**, *13*, 331–343, doi:10.1002/ldr.516.
49. de Castilho, C. V.; Magnusson, W. E.; de Araújo, R. N. O.; Luizão, R. C. C.; Luizão, F. J.; Lima, A. P.; Higuchi, N. Variation in aboveground tree live biomass in a central Amazonian Forest: Effects of soil and topography. *For. Ecol. Manage.* **2006**, *234*, 85–96, doi:10.1016/j.foreco.2006.06.024.
50. Chave, J.; Andalo, C.; Brown, S.; Cairns, M. A.; Chambers, J. Q.; Eamus, D.; Fölster, H.; Fromard, F.; Higuchi, N.; Kira, T.; Lescure, J.-P.; Nelson, B. W.; Ogawa, H.; Puig, H.; Riéra, B.; Yamakura, T. Tree allometry and improved estimation of carbon stocks and balance in tropical forests. *Oecologia* **2005**, *145*, 87–99, doi:10.1007/s00442-005-0100-x.
51. IBGE - Instituto Brasileiro de Geografia e Estatística *Manual Técnico da Vegetação Brasileira. 2ª edição revista e ampliada. Sistema Fitogeográfico. Inventário das Formações Florestais e Campestres. Técnicas e Manejo de Coleções Botânicas. Procedimentos para Mapeamentos.*; 2012; ISBN 9788524042720.
52. Prates-Clark, C. da C.; Lucas, R. M.; dos Santos, J. R. Implications of land-use history for forest regeneration in the Brazilian Amazon. *Can. J. Remote Sens.* **2009**, *35*, 534–553, doi:10.5589/m10-004.
53. Vieira, S.; Trumbore, S.; Camargo, P. B.; Selhorst, D.; Chambers, J. Q.; Higuchi, N.; Martinelli, L. A. Slow growth rates of Amazonian trees: Consequences for carbon cycling. *Proc. Natl. Acad. Sci.* **2005**, *102*, 18502–18507, doi:10.1073/pnas.0505966102.
54. Pyle, E. H.; Santoni, G. W.; Nascimento, H. E. M.; Hutyra, L. R.; Vieira, S.; Curran, D. J.; van Haren, J.; Saleska, S. R.; Chow, V. Y.; Carmago, P. B.; Laurance, W. F.; Wofsy, S. C. Dynamics of carbon, biomass, and structure in two Amazonian forests. *J. Geophys. Res. Biogeosciences* **2008**, *113*, n/a-n/a, doi:10.1029/2007JG000592.
55. Hunter, M. O.; Keller, M.; Morton, D.; Cook, B.; Lefsky, M.; Ducey, M.; Saleska, S.; de Oliveira, R. C.; Schietti, J. Structural Dynamics of Tropical Moist Forest Gaps. *PLoS One* **2015**, *10*, e0132144, doi:10.1371/journal.pone.0132144.
56. Silva, C. V. de J. Caracterização florístico-estrutural e modelagem de biomassa na floresta amazônica a partir de dados ALOS/PALSAR e TERRASAR/TANDEM-X, Instituto Nacional de Pesquisas Espaciais, 2014.
57. Silva, C. V. de J.; Santos, J. R. dos; Galvão, L. S.; Silva, R. D. da; Moura, Y. M. Floristic and structure of an Amazonian primary forest and a chronosequence of secondary succession. *Acta Amaz.* **2016**, *46*, 133–150, doi:10.1590/1809-4392201504341.
58. Cassol, H. L. G.; Shimabukuro, Y. E.; Carreiras, J. M. D. B.; Moraes, E. C. Improved tree height estimation of secondary forests in the Brazilian Amazon. *Acta Amaz.* **2018**, *48*, 179–190.
59. Cassol, H. L. G.; Tese Aplicação Dos Dados Polarimétricos Alos / Palsar-2 Para Modelagem De Biomassa, Instituto Nacional de Pesquisas Espaciais (INPE), 2017.
60. Chave, J.; Réjou-Méchain, M.; Búrquez, A.; Chidumayo, E.; Colgan, M. S.; Delitti, W. B. C.; Duque, A.; Eid, T.; Fearnside, P. M.; Goodman, R. C.; Henry, M.; Martínez-Yrízar, A.; Mugasha, W. A.; Muller-Landau, H. C.; Mencuccini, M.; Nelson, B. W.; Ngomanda, A.; Nogueira, E. M.; Ortiz-Malavassi, E.; Pélissier, R.; Ploton, P.; Ryan, C. M.; Saldarriaga, J. G.; Vieilledent, G. Improved allometric models to estimate the aboveground biomass of tropical trees. *Glob. Chang. Biol.* **2014**, *20*, 3177–3190, doi:10.1111/gcb.12629.

61. Zanne, A. E.; Lopez-Gonzalez, G.; Coomes, D. A. A.; Ilic, J.; Jansen, S.; Lewis, S. L. S. L.; Miller, R. B. B.; Swenson, N. G. G.; Wiemann, M. C. C.; Chave, J. Global wood density database. *Dryad* **2009**, *235*, 33, doi:10.5061/dryad.234/1.
62. Brown, S.; Gillespie, A. J. R.; Lugo, A. E. Biomass estimation methods for tropical forests with applications to forest inventory data. *For. Sci.* 1989, *35*, 881–902.
63. Tiepolo, G.; Calmon, M.; Rocha Feretti, a Measuring and Monitoring Carbon Stocks at the Guaraqueçaba Climate Action Report, Paraná, Brazil. *Ext. Ser.* **2002**, *153*, 98–115.
64. Goodman, R. C.; Phillips, O. L.; del Castillo Torres, D.; Freitas, L.; Cortese, S. T.; Monteagudo, A.; Baker, T. R. Amazon palm biomass and allometry. *For. Ecol. Manage.* **2013**, *310*, 994–1004, doi:10.1016/j.foreco.2013.09.045.
65. Cummings, D. L.; Boone Kauffman, J.; Perry, D. A.; Flint Hughes, R. Aboveground biomass and structure of rainforests in the southwestern Brazilian Amazon. *For. Ecol. Manage.* **2002**, *163*, 293–307, doi:10.1016/S0378-1127(01)00587-4.
66. Uhl, A. C.; Buschbacher, R.; Serrao, E. a S.; Uhl, C.; Buschbachertt, R. Abandoned Pastures in Eastern Amazonia . I . Patterns of Plant Succession. *J. Ecol.* **1988**, *76*, 663–681.
67. Draper, N. R.; Smith, H. **Applied regression analysis**. 2 ed. New York: John Wiley. 709 p.; 1981; ISBN: 978-0-471-17082-2.
68. Luckman, A.; Baker, J.; Kuplich, T. M.; Freitas, C. C.; Frery, A. C. A study of the relationship between radar backscatter and regenerating tropical forest biomass for spaceborne SAR instruments. *Remote Sens. Environ.* **1997**, *60*, 1–13, doi:10.1016/S0034-4257(96)00121-6.
69. Prates-Clark, C. C. Remote sensing of tropical regenerating forests in the Brazilian Amazon, 2004.
70. Santos, J. Airborne P-band SAR applied to the aboveground biomass studies in the Brazilian tropical rainforest. *Remote Sens. Environ.* **2003**, *87*, 482–493, doi:10.1016/j.rse.2002.12.001.
71. Robinson, A. P.; Hamann, J. D. *Forest Analytics with R*; Gentleman, R., Hornik, K., Parmigiani, G., Eds.; Springer New York: New York, NY, 2011; ISBN 978-1-4419-7761-8.
72. Neter, J.; Kutner, N. H.; Nachtssheim, C. J.; Wasserman,W. Applied linear statistical models. (4 ed.). Boston, MA: McGraw- Hill. 1408 p, 1996.
73. Baker, T. R.; Phillips, O. L.; Malhi, Y.; Almeida, S.; Arroyo, L.; Di Fiore, A.; Erwin, T.; Killeen, T. J.; Laurance, S. G.; Laurance, W. F.; Lewis, S. L.; Lloyd, J.; Monteagudo, A.; Neill, D. a.; Patino, S.; Pitman, N. C. A.; M. Silva, J. N.; Vasquez Martinez, R. Variation in wood density determines spatial patterns inAmazonian forest biomass. *Glob. Chang. Biol.* **2004**, *10*, 545–562, doi:10.1111/j.1365-2486.2004.00751.x.
74. Chambers, J. Q.; Santos, J. dos; Ribeiro, R. J.; Higuchi, N. Tree damage, allometric relationships, and above-ground net primary production in central Amazon forest. *For. Ecol. Manage.* **2001**, *152*, 73–84, doi:10.1016/S0378-1127(00)00591-0.
75. De Oliveira, A. A.; Mori, S. A. A central Amazonian terra firme forest. I. High tree species richness on poor soils. *Biodivers. Conserv.* **1999**, *8*, 1219–1244, doi:10.1023/A:1008908615271.
76. Espírito-Santo, F. D. B. Caracterização e mapeamento da vegetação da região da Floresta Nacional do Tapajós através de dados óticos, radar e inventários florestais, Instituto Nacional de Pesquisas Espaciais, 2003.
77. Holm, J. A.; Chambers, J. Q.; Collins, W. D.; Higuchi, N. Forest response to increased disturbance in the central Amazon and comparison to western Amazonian forests. *Biogeosciences* **2014**, *11*, 5773–5794, doi:10.5194/bg-11-5773-2014.
78. Hunter, M. O.; Keller, M.; Victoria, D.; Morton, D. C. Tree height and tropical forest biomass estimation. *Biogeosciences* **2013**, *10*, 8385–8399, doi:10.5194/bg-10-8385-2013.
79. Malhi, Y.; Wood, D.; Baker, T. R.; Wright, J.; Phillips, O. L.; Cochrane, T.; Meir, P.; Chave, J.; Almeida, S.; Arroyo, L.; Higuchi, N.; Killeen, T. J.; Laurance, S. G.; Laurance, W. F.; Lewis, S. L.; Monteagudo, A.; Neill, D. A.; Vargas, P. N.; Pitman, N. C. A.; Quesada, C. A.; Salomao, R.; Silva, J. N. M.; Lezama, A. T.; Terborgh, J.; Martinez, R. V.; Vinceti, B. The regional variation of aboveground live biomass in old-growth Amazonian forests. *Glob. Chang. Biol.* **2006**, *12*, 1107–1138, doi:10.1111/j.1365-2486.2006.01120.x.
80. Magnabosco Marra, D.; Higuchi, N.; Trumbore, S. E.; Ribeiro, G. H. P. M.; dos Santos, J.; Carneiro, V. M. C.; Lima, A. J. N.; Chambers, J. Q.; Negrón-Juárez, R. I.; Holzwarth, F.; Reu, B.; Wirth, C. Predicting biomass of hyperdiverse and structurally complex central Amazonian forests – a virtual approach using extensive field data. *Biogeosciences* **2016**, *13*, 1553–1570, doi:10.5194/bg-13-1553-2016.

81. Milliken, W. Structure and Composition of One Hectare of Cental Amazonian Terra Firme Forest. *Biotropica* **1998**, *30*, 530–537.
82. Narvaes, I. D. S. Avaliação de dados SAR polarimétricos para estimativa de biomassa em diferentes fitofisionomias de florestas tropicais, Instituto Nacional de Pesquisas Espaciais, 2010.
83. Nascimento, H. E. M.; Laurance, W. F. Total aboveground biomass in central Amazonian rainforests: A landscape-scale study. *For. Ecol. Manage.* **2002**, *168*, 311–321, doi:10.1016/S0378-1127(01)00749-6.
84. Rankin-de-Mérona, J. M.; Prance, G. T.; Hutchings, R. W.; Freitas da Silva, M.; Rodrigues, W. A.; Uehling, M. E. Preliminary results of a large-scale tree inventory of upland rain forest in the central Amazon. *Acta Amaz.* **1992**, *22*, 493–534.
85. Suwa, R.; Sakai, T.; Santos, J. Dos; Silva, R. P. Da; Kajimoto, T.; Ishizuka, M.; Higuchi, N. Significance of Topographic Gradient in Stem Diameter - Height Allometry for Precise Biomass Estimation of a Tropical Moist Forest in the Central Amazon. *Japan Agric. Res. Q. JARQ* **2013**, *47*, 109–114, doi:10.6090/jarq.47.109.
86. Keller, M.; Palace, M.; Hurtt, G. Biomass estimation in the Tapajos National Forest, Brazil. *For. Ecol. Manage.* **2001**, *154*, 371–382, doi:10.1016/S0378-1127(01)00509-6.
87. Pretzsch, H. *Forest Dynamics, Growth and Yield*; Springer Berlin Heidelberg: Berlin, Heidelberg, 2010; ISBN 978-3-540-88306-7.
88. JAXA. Japan Aerospace Exploration Agency ALOS/PALSAR-2. Tokyo, Japan, 2015. Available online: http://global.jaxa.jp/projects/sat/ALOS2/pdf/daichi2_e.pdf. (Accessed on 15 Apr. 2015).
89. INSTITUTO NACIONAL DE METEOROLOGIA (INMET). Historic data precipitation. Available online: http://www.inmet.gov.br/portal/index.php?r=home2/index. (accessed on 20 May 2017).
90. Freeman, A.; Saatchi, S. S. On the detection of Faraday rotation in linearly polarized L-band SAR backscatter signatures. *IEEE Trans. Geosci. Remote Sens.* **2004**, *42*, 1607–1616, doi:10.1109/TGRS.2004.830163.
91. EMBRACE/INPE. TEC map. Available online: http://www2.inpe.br/climaespacial/portal/tec-map-home/. (Accessed on 20 Feb. 2017).
92. Wright, P. A.; Quegan, S.; Wheadon, N. S.; Hall, C. D. Faraday rotation effects on l-band spaceborne sar data. *IEEE Trans. Geosci. Remote Sens.* **2003**, *41*, 2735–2744, doi:10.1109/TGRS.2003.815399.
93. Curlander, J. C. Location of Spaceborne Sar Imagery. *IEEE Trans. Geosci. Remote Sens.* **1982**, *GE-20*, 359–364, doi:10.1109/TGRS.1982.350455.
94. Small, D.; Schubert, A. *Guide to ASAR Geocoding*; Zurich, Switzerland, 2008;
95. Mermoz, S.; Réjou-Méchain, M.; Villard, L.; Le Toan, T.; Rossi, V.; Gourlet-Fleury, S. Decrease of L-band SAR backscatter with biomass of dense forests. *Remote Sens. Environ.* **2015**, *159*, 307–317, doi:10.1016/j.rse.2014.12.019.
96. Hall, M. Correlation-based Feature Selection for Machine Learning, University of Waikato, 1999.
97. Romanski, P.; Kotthoff, L. *FSelector: Selecting Attributes*. R package version 0.31. https://CRAN.R-project.org/package=FSelector. 2015.
98. Yang, Y.; Pedersen, J. O. A comparative study on feature selection in text categorization. In *ICML '97 Proceedings of the Fourteenth International Conference on Machine Learning*; Morgan Kaufmann Publishers Inc., Ed.; San Francisco, CA, USA, 1997; pp. 412–420.
99. Parimala, R.; Nallaswamy, R. A Study of Spam E-mail classification using Feature Selection package. *Glob. J. Comput. Sci. Technol.* **2011**, *11*, 45–54.
100. Hastie, T.; Tibshirani, R.; Friedman, J. *The elements of statistical learning: data mining, inference, and prediction*. 2. ed. Stanford, CA: Springer, 2009. 745 p.
101. Calcagno, V. Glmulti*: Model selection and multimodel inference made easy*. R package version 1.0.7. https://CRAN.R-project.org/package=glmulti. 2013.
102. Santoro, M.; Eriksson, L.; Schmullius, C.; Wiesmann, A. Seasonal and topographic effects on growing stock volume estimates from JERS-1 backscatter in Siberian forests. In *EARSeL Annual Symposium*; 2003.
103. Lebrija-Trejos, E.; Bongers, F.; Pérez-García, E. A.; Meave, J. A. Successional Change and Resilience of a Very Dry Tropical Deciduous Forest Following Shifting Agriculture. *Biotropica* **2008**, *40*, 422–431, doi:10.1111/j.1744-7429.2008.00398.x.

104. Holm, J. A.; Chambers, J. Q.; Collins, W. D.; Higuchi, N. Forest response to increased disturbance in the central Amazon and comparison to western Amazonian forests. *Biogeosciences* **2014**, *11*, 5773–5794, doi:10.5194/bg-11-5773-2014.
105. Houghton, R. A.; Skole, D. L.; Nobre, C. A.; Hackler, J. L.; Lawrence, K. T.; Chomentowski, W. H. Annual fluxes of carbon from deforestation and regrowth in the Brazilian Amazon. *Nature* **2000**, *403*, 301–304, doi:10.1038/35002062.
106. Jakovac, C. C.; Pe?a-Claros, M.; Kuyper, T. W.; Bongers, F. Loss of secondary-forest resilience by land-use intensification in the Amazon. *J. Ecol.* **2015**, *103*, 67–77, doi:10.1111/1365-2745.12298.
107. Poorter, L.; Bongers, F.; Aide, T. M.; Almeyda Zambrano, A. M.; Balvanera, P.; Becknell, J. M.; Boukili, V.; Brancalion, P. H. S.; Broadbent, E. N.; Chazdon, R. L.; Craven, D.; de Almeida-Cortez, J. S.; Cabral, G. A. L.; de Jong, B. H. J.; Denslow, J. S.; Dent, D. H.; DeWalt, S. J.; Dupuy, J. M.; Durán, S. M.; Espírito-Santo, M. M.; Fandino, M. C.; César, R. G.; Hall, J. S.; Hernandez-Stefanoni, J. L.; Jakovac, C. C.; Junqueira, A. B.; Kennard, D.; Letcher, S. G.; Licona, J.-C.; Lohbeck, M.; Marín-Spiotta, E.; Martínez-Ramos, M.; Massoca, P.; Meave, J. A.; Mesquita, R.; Mora, F.; Muñoz, R.; Muscarella, R.; Nunes, Y. R. F.; Ochoa-Gaona, S.; de Oliveira, A. A.; Orihuela-Belmonte, E.; Peña-Claros, M.; Pérez-García, E. A.; Piotto, D.; Powers, J. S.; Rodríguez-Velázquez, J.; Romero-Pérez, I. E.; Ruíz, J.; Saldarriaga, J. G.; Sanchez-Azofeifa, A.; Schwartz, N. B.; Steininger, M. K.; Swenson, N. G.; Toledo, M.; Uriarte, M.; van Breugel, M.; van der Wal, H.; Veloso, M. D. M.; Vester, H. F. M.; Vicentini, A.; Vieira, I. C. G.; Bentos, T. V.; Williamson, G. B.; Rozendaal, D. M. A. Biomass resilience of Neotropical secondary forests. *Nature* **2016**, *530*, 211–214, doi:10.1038/nature16512.
108. Saatchi, S.; Marlier, M.; Chazdon, R. L.; Clark, D. B.; Russell, A. E. Impact of spatial variability of tropical forest structure on radar estimation of aboveground biomass. *Remote Sens. Environ.* **2011**, *115*, 2836–2849, doi:10.1016/j.rse.2010.07.015.
109. Ahmed, R.; Siqueira, P.; Hensley, S. Analyzing the uncertainty of biomass estimates from l-band radar backscatter over the harvard and howland forests. *IEEE Trans. Geosci. Remote Sens.* **2014**, *52*, 3568–3586, doi:10.1109/TGRS.2013.2273738.
110. Joshi, N.; Mitchard, E.; Schumacher, J.; Johannsen, V.; Saatchi, S.; Fensholt, R. L-Band SAR Backscatter Related to Forest Cover, Height and Aboveground Biomass at Multiple Spatial Scales across Denmark. *Remote Sens.* **2015**, *7*, 4442–4472, doi:10.3390/rs70404442.
111. Woodhouse, I. H. *Introduction to microwave remote sensing*. Boca Raton: Taylor & Francis Group CRC Press, 2006. p. 370. ISBN: 0-415-27123-1.
112. Lee, J.-S.; Pottier, E. *Polarimetric radar imaging: from basics to applications*. CRC Press: Taylor & Francis Group New York, USA, 2009. 440 p. ISBN 978-1-4200- 5497-2.
113. Zhang, L.; Zou, B.; Cai, H.; Zhang, Y. Multiple-Component Scattering Model for Polarimetric SAR Image Decomposition. *IEEE Geosci. Remote Sens. Lett.* **2008**, *5*, 603–607, doi:10.1109/LGRS.2008.2000795.
114. Martins, F. da S. R. V. Caracterização e estimativa de biomassa aérea de florestas atingidas pelo fogo a partir de imagens polarimétricas ALOS/PALSAR, Instituto Nacional de Pesquisas Espaciais - INPE, 2012.
115. Lee, J.; Ainsworth, T. L. The Effect of Orientation Angle Compensation on Coherency Matrix and Polarimetric Target Decompositions. *IEEE Trans. Geosci. Remote Sens.* **2011**, *49*, 53–64, doi:10.1109/TGRS.2010.2048333.
116. Kumar, S.; Khati, U. G.; Chandola, S.; Agrawal, S.; Kushwaha, S. P. S. Polarimetric SAR Interferometry based modeling for tree height and aboveground biomass retrieval in a tropical deciduous forest. *Adv. Sp. Res.* **2017**, *60*, 571–586, doi:10.1016/j.asr.2017.04.018.
117. Freeman, A.; Durden, S. L. A three-component scattering model for polarimetric SAR data. *IEEE Trans. Geosci. Remote Sens.* **1998**, *36*, 963–973, doi:10.1109/36.673687.
118. Neumann, M. Remote sensing of vegetation using multi-baseline polarimetric SAR interferometry : theoretical modeling and physical parameter retrieval, 2009.
119. van Zyl, J. J. Application of Cloude's target decomposition theorem to polarimetric imaging radar data. In *SPIE conference on Radar Polarimetry*; Mott, H., Boerner, W.-M., Eds.; San Diego '92, 1992, San Diego, CA, United States, 1993; Vol. 1748, p. 184.
120. Yamaguchi, Y.; Moriyama, T.; Ishido, M.; Yamada, H. Four-component scattering model for polarimetric SAR image decomposition. *IEEE Trans. Geosci. Remote Sens.* **2005**, *43*, 1699–1706, doi:10.1109/TGRS.2005.852084.

121. Bhattacharya, A.; Muhuri, A.; De, S.; Manickam, S.; Frery, A. C. Modifying the Yamaguchi Four-Component Decomposition Scattering Powers Using a Stochastic Distance. *IEEE J. Sel. Top. Appl. Earth Obs. Remote Sens.* **2015**, *8*, 3497–3506, doi:10.1109/JSTARS.2015.2420683.
122. Singh, G.; Yamaguchi, Y.; Park, S.-E. General Four-Component Scattering Power Decomposition With Unitary Transformation of Coherency Matrix. *IEEE Trans. Geosci. Remote Sens.* **2013**, *51*, 3014–3022, doi:10.1109/TGRS.2012.2212446.
123. Touzi, R. Target scattering decomposition of one-look and multi-look SAR data using a new coherent scattering model: the TSVM. In *IEEE International IEEE International IEEE International Geoscience and Remote Sensing Symposium, 2004. IGARSS '04. Proceedings. 2004*; IEEE, 2004; Vol. 4, pp. 2491–2494.
124. Cloude, S.; Pottier, E. An entropy based classification scheme for land applications of polarimetric SAR. *IEEE Trans. Geosci. Remote Sens.* **1997**, *35*, 68–78, doi:10.1109/36.551935.
125. Huynen, J. R. Phenomenological theory of radar targets, 1970.
126. Cloude, S. R. Target decomposition theorems in radar scattering. *Electronics Letters*, **1985**, 21, 22–24.
127. Holm, W. A.; Barnes, R. M. On radar polarization mixed target state decomposition techniques. In *Proceedings of the 1988 IEEE National Radar Conference*; IEEE, 1988; pp. 249–254.
128. Réfrégier, P.; Morio, J. Shannon entropy of partially polarized and partially coherent light with Gaussian fluctuations. *J. Opt. Soc. Am. A. Opt. Image Sci. Vis.* **2006**, *23*, 3036–44, doi:117913 [pii].
129. Allain, S.; Ferro-Famil, L.; Pottier, E. New Eigenvalue-Based Parameters for Natural Media Characterization. In *European Radar Conference, 2005. EURAD 2005.*; IEEE, 2005; Vol. 2005, pp. 197–200.
130. Durden, S. L.; van Zyl, J. J.; Zebker, H. A. The unpolarized component in polarimetric radar observations of forested areas. *IEEE Trans. Geosci. Remote Sens.* **1990**, *28*, 268–271, doi:10.1109/36.46706.
131. Ainsworth, T. L.; Lee, J. S.; Schuler, D. L. Multi-frequency polarimetric SAR data analysis of ocean surface features. In *IGARSS 2000. IEEE 2000 International Geoscience and Remote Sensing Symposium. Taking the Pulse of the Planet: The Role of Remote Sensing in Managing the Environment. Proceedings (Cat. No.00CH37120)*; IEEE: Honolulu, HI, USA, 2000; Vol. 3, pp. 1113–1115.
132. Pope, K. O.; Rey-Benayas, J. M.; Paris, J. F. Radar remote sensing of forest and wetland ecosystems in the Central American tropics. *Remote Sens. Environ.* **1994**, *48*, 205–219, doi:10.1016/0034-4257(94)90142-2.
133. Saatchi, S.S.; Dubayah, R.; Clark, D.; Chazdon, R.; Hollinger, D. Estimation of forest biomass change from fusion of radar and lidar measurements. In: SEMINÁRIO DE ATUALIZAÇÃO EM SENSORIAMENTO REMOTO E SISTEMAS DE INFORMAÇÕES GEOGRÁFICAS APLICADOS À ENGENHARIA FLORESTAL, 9 (SENGEF, 2010), Curitiba, Brasil. Apresentação... Disponível em: <http://www.slideshare.net/grssieee/estimation-of-forest-biomass>.
134. Henderson, F. M.; Lewis, A. J. *Manual of remote sensing: principles and applications of imaging radar*. 3. ed. John Wiley Sons, New York, USA, 1998. 896 p.